PHYSICAL REVIEW B VOLUME 47, NUMBER 18 1 MAY 1993-II

Doping states in the two-dimensional three-band Peierls-Hubbard model

K. Yonemitsu* and A. R. Bishop
Theoretical Division, Los Alamos National Laboratory, Los Alamos, New Mexico 87545

J. Lorenzana†
International School for Advanced Studies, Strada Costiera 11, 34014 Trieste, Italy
(Received 24 September 1992)

Doping states in a two-dimensional three-band Peierls-Hubbard model for the copper oxides are investigated with inhomogeneous Hartree-Fock (HF) and random-phase approximations. The doping states are sensitive to small changes of interaction parameters because they easily change *local* energy balance between different interactions around added holes. For the parameter values derived from constrained-density-functional methods for the copper oxides, added holes form isolated small ferromagnetic polarons. When the parameters are varied around these values, different types of doping states are obtained: For stronger on-site repulsion at Cu sites, larger ferromagnetic polarons are formed, which are qualitatively different from the small polarons; for stronger nearest-neighbor Cu-O repulsion, polarons are clumped or there occurs phase separation into Cu- and O-hole-rich regions; *intersite* electron-lattice coupling rapidly changes the small polarons by quenching a Cu magnetic moment and *locally* distorting the lattice in an otherwise undistorted antiferromagnetic background. This is regarded as a rapid crossover from a Zhang-Rice singlet to a covalent molecular singlet, and occurs substantially below a critical strength for destruction of the stoichiometric antiferromagnetic state. However *intrasite* electron-lattice coupling, in contrast to the intersite coupling, does not dramatically affect the hole-doping states. Doping induces modes in magnetic, optical, and vibronic response functions. Local infrared-active phonon modes are induced in infrared absorption spectra for finite electron-lattice coupling. They are correlated with doping-induced particle-hole excitations observed in optical absorption spectra and in magnetic excitation spectra. These doping-induced particle-hole excitations are associated with the local HF eigenstates in the charge-transfer gap. Each doping state has distinctive excitation spectra in the magnetic, optical, and vibronic channels. In particular, the hole-doping states with small polarons have doping-induced, infrared absorption peaks on the low-frequency side of the stoichiometric peak, while the electron-doping states have them on the high-frequency side.

I. INTRODUCTION

A considerable amount of the modeling of high-temperature superconductors has focused on the identification of hole-doping states (spin bags, polarons, excitons) defined with respect to stoichiometric antiferromagnetic (AF) two-dimensional (2D) Cu-O ground states.[1] Many discussions have emphasized the 2D one-band Hubbard model;[2] others have included multiband aspects[3–5] and more occasionally additional interactions such as electron lattice,[6,7] extended orbitals,[8] or 3D coupling. The purpose of this paper is to demonstrate that the nature of doping states and their interactions can indeed be extremely sensitive to effects going beyond a pure 2D one-band Hubbard model and that doping states can be identified by their spectroscopic signatures. Recently, we reported this feature in a Letter.[9] Here we present results for a variety of parameter values and a more detailed explanation and discussion of the method. The electronic part of the model is a standard one,[3–5] and its lattice part includes only displacements of planar O atoms along the Cu-O bonds for simplicity.

Specifically, we report here the following for parameter values in regimes relevant to the copper oxides: (i) U_d (the electron-electron interaction on Cu sites) beyond a critical strength, with renormalized site-energy difference between Cu and O sites kept fixed, induces a transition from *small* ferromagnetic polarons, primarily on a single Cu site and four surrounding O sites, to *intermediate-size* ferromagnetic polarons, whose spin densities are perpendicular to the AF background. (ii) Hole doping in the presence of U_{pd} (the electron-electron interaction between neighboring Cu and O sites) beyond a critical strength, with renormalized site-energy difference kept fixed, produces phase separation[10–12] into undoped AF regions of Cu holes and doped regions of charge transfer to O sites. Near to but smaller than the critical strength, polarons are clumped. (iii) Coupling with the planar O-atom displacements through the hopping integral ("intersite" electron-lattice coupling λ_α) triggers a highly nonlinear feedback mechanism. This feedback rapidly changes the small polarons by quenching a Cu magnetic moment and *locally* distorting the lattice in an otherwise undistorted AF background, substantially

below a critical strength for destruction of the stoichiometric AF state. (iv) Coupling with the planar O-atom displacements through the Cu-site energy ("intrasite" electron-lattice coupling λ_β) does not rapidly affect the hole-doping states. The effect of intersite electron-lattice coupling is so significant that it can overcome the effect of U_d *locally*; i.e., for large U_d, the intermediate-size polarons are replaced by small polarons. In addition, it enhances phase separation for large U_{pd}.

Nuñez Regueiro and Aligia have investigated similar 2D and 3D Peierls-Hubbard models at strong coupling with perturbation theory in the hopping strength.[6] They have considered the same intrasite electron-lattice coupling as our λ_β coupling [see text below Eq. (3)] and also modulation of the nearest-neighbor Cu-O repulsion by an O-atom displacement. The lattice effect was studied in a regime where the stoichiometric state is a charge-density-wave state. We found that hole-doping states are insensitive to the intrasite electron-lattice coupling, which is consistent with their work in a sense. On the other hand, our study goes beyond their study in two respects: First the self-consistent method we use is not perturbative, and second we include *intersite* electron-lattice coupling (λ_α). As we will see later, nonlinear (i.e., nonperturbative) effects concerning the intersite electron-lattice coupling are very important in the hole-doping states we found. As a result, the hole-doping states in the AF background are very sensitive to the intersite electron-lattice coupling. This sensitivity does not depend on whether the nearest-neighbor Cu-O repulsion is large or small. For our result, finiteness of the on-site repulsion at Cu sites is important so that the local quenching of a Cu magnetic moment occurs with local lattice distortion. Therefore the slave-boson technique[8] is inappropriate as far as it assumes infinite strength for on-site repulsions or homogeneous renormalization of model parameters. Concerning sensitivity of doping states to electron-lattice coupling, Zhong and Schüttler have recently shown in the nearly half-filled 2D one-band Holstein-Hubbard model that the presence of AF spin correlations can cause polaronic carrier self-localization.[7] This also occurs at moderate electron-lattice coupling, not close to any structural instabilities. Such local relaxation around additional holes has also been incorporated with *ab initio* local-density-functional methods.[13,14]

Doping induces new modes in magnetic, optical, and vibronic response functions. In the presence of electron-lattice coupling, there appear doping-induced, local infrared- (IR-) active phonon modes. These are seen as doping-induced peaks in IR absorption spectra and are correlated with doping-induced particle-hole excitations observed in optical absorption spectra and in magnetic excitation spectra. These doping-induced particle-hole excitations are associated with the local Hartree-Fock (HF) eigenstates in the charge-transfer gap. For the above doping states, optical and IR absorption spectra and magnetic excitation spectra are quite distinct. These spectroscopic and magnetic signatures should help to identify the chemical doping states[15] and the photoinduced doping states[16] reported in the CuO_2 planes of high-T_c materials. We will see below that the hole-doping states with small polarons have doping-induced IR absorption peaks on the low-frequency side of the stoichiometric peak, while the electron-doping states have them on the high-frequency side.[9]

The essential feature in all of the above observations is that doping into a highly commensurate ground state in the presence of competing interactions and order parameters (spin density wave, charge density wave, charge transfer) typically results in polaronic local distortions which *share* the character of all the order parameters to some degree. This is a local "coexistence" in the global environment of the undoped homogeneous single-order-parameter phase. In addition, the *multiband* Peierls-Hubbard model with extended interactions introduces not only global coexistence (e.g., spin-Peierls) possibilities,[17,18] but also the feature of localized *or* somewhat extended doping states, depending on parameter values. Indeed, in appropriate parameter regimes, dynamical exchange between localized and extended charge or spin distributions can be anticipated (see Figs. 1 and 3 below). Of course, if an interaction is strong enough, it dominates the global order parameter structure, but doping regions can be strongly affected at much weaker values. Thus, as in the present study, strong on-site Hubbard coupling may drive a global AF order, but electron-lattice interactions can be dominant in the neighborhood of added holes.

In view of the inhomogeneities anticipated in the above discussions, we have used a HF technique for the electronic part, totally unrestricted in both spin *and* direct space[19–22] — for our problems, this is superior to traditional homogeneous HF approaches — and a classical treatment for the lattice part. To these generally inhomogeneous HF configurations, we have added a similarly inhomogeneous random-phase-approximation (RPA) analysis of linear fluctuations to calculate dynamic magnetic susceptibility, optical absorption, and IR absorption. This method has the advantage of flexibility (it allows us easily to vary several interactions and parameters in the 2D three-band extended Peierls-Hubbard model) compared with computing-intensive methods such as exact diagonalization or quantum Monte Carlo methods. At the same time, comparisons with exact finite-system studies[4,23] have demonstrated substantial qualitative success for our approach in the 2D three-band Hubbard model[22] and in a 1D two-band spinless fermion model.[24] This success of an inhomogeneous HF plus RPA approach is the result of a much superior basis set for strongly localized polaronic states as compared to traditional homogeneous (HF plus) RPA methods which are limited to a spatially extended plane-wave basis. The inhomogeneous RPA basis automatically describes local shape-oscillation modes well, and these dominate interesting quasiparticle response properties. On the other hand, the major failing is that symmetries (e.g., spin rotation or translation) are broken, whereas they are automatically preserved in the weak-coupling homogeneous (HF plus) RPA regime. Thus the methods are complementary, but our inhomogeneous approach is most appropriate to short-length and short-time scale issues at strong coupling, where the broken symmetry is approxi-

mately valid.

The outline of this paper is as follows. In Sec. II, the model and the parameters used in this paper are presented. In Sec. III, mean-field states are presented for a variety of parameter values. It is shown how small changes of interaction parameters strongly modify the character of doping states and the static interaction potentials among them. In Sec. IV, RPA excitation spectra in magnetic, optical, and vibronic channels are presented for small-polaron states along with HF spectra for single-hole excitations. It is also shown that the adiabatic approximation works excellently for the IR absorption spectra. Then, in Sec. V, the IR absorption spectra are obtained in the adiabatic approximation and presented for hole- and electron-doping states. Relevance to experimental data is discussed. Summary and conclusions are presented in Sec. VI. All technical details are described in the Appendixes.

II. MODEL AND PARAMETERS

We consider a 2D three-band extended Peierls-Hubbard model, including both electron-electron and electron-phonon interactions:

$$H = \sum_{i\neq j,\sigma} t_{ij}(\{u_k\})c^\dagger_{i\sigma}c_{j\sigma} + \sum_{i,\sigma} e_i(\{u_k\})c^\dagger_{i\sigma}c_{i\sigma} + \sum_i U_i c^\dagger_{i\uparrow}c^\dagger_{i\downarrow}c_{i\downarrow}c_{i\uparrow} + \sum_{\langle i\neq j\rangle,\sigma,\sigma'} U_{ij}c^\dagger_{i\sigma}c^\dagger_{j\sigma'}c_{j\sigma'}c_{i\sigma} + \sum_l \frac{1}{2M_l}p_l^2 + \sum_{k,l}\frac{1}{2}K_{kl}u_k u_l \quad , \tag{1}$$

where the operator $c^\dagger_{i\sigma}$ creates a *hole* of spin σ at site i in the Cu $d_{x^2-y^2}$ or the O $p_{x,y}$ orbital. We assume the parameters for the one-fermion operators, hopping integrals $t_{ij}(\{u_k\})$ between sites i and j and site-diagonal energies $e_i(\{u_k\})$ at site i, depend linearly on lattice displacements u_k with coefficients $\bar{g}^k_{ij}$ and $\bar{g}^k_{ii}$, respectively,

$$t_{ij}(\{u_k\}) = t^0_{ij} + \sum_k \bar{g}^k_{ij}u_k \quad , \tag{2}$$

$$e_i(\{u_k\}) = e^0_i + \sum_k \bar{g}^k_{ii}u_k \quad . \tag{3}$$

Holes repel each other with strength U_i on site i and strength U_{ij} between different sites i and j. Displacements of atoms and their conjugate momenta are denoted by u_l and p_l, respectively. The quantity M_l stands for the ionic mass at site l and K_{kl} for the spring constant between the ions at sites k and l. The symbol $\langle i \neq j\rangle$ under the summation symbol means that a pair (i,j) is counted only once.

In this paper, we consider the nearest-neighbor Cu-O (t_{pd}) and O-O ($-t_{pp}$) hoppings for t^0_{ij}, Cu-site (ϵ_d) and O-site (ϵ_p) energies for e^0_i, with $\Delta = \epsilon_p - \epsilon_d$, Cu-site ($U_d$) and O-site ($U_p$) repulsions for U_i, and the nearest-neighbor Cu-O repulsion (U_{pd}) for U_{ij}. For the lattice part, we study only the displacements of planar O atoms along the Cu-O bonds. (We take the Cu atoms to be fixed, for simplicity.) Furthermore, we assume that only diagonal components of the spring-constant matrix are finite, $K_{kl} = \delta_{k,l}K$. For electron-lattice coupling, we assume that the nearest-neighbor Cu-O hopping is modified by the O-atom displacement u_k, linearly with coefficient α, $t_{ij}(\{u_k\}) = t_{pd} - \alpha u_k$, if the Cu-O bond becomes longer with positive u_k, or $t_{pd}+\alpha u_k$ if the bond becomes shorter. The Cu-site energy is assumed to be modulated by the displacements of the four surrounding O atoms, u_k, linearly with coefficient β, $e_i(\{u_k\}) = \epsilon_d + \beta\sum_k(\pm u_k)$, where the sign takes "+" if the bond becomes longer with positive u_k or "−" if the bond becomes shorter.

Parameter values are used in regimes relevant to the copper oxides. As a reference parameter set, we use $t_{pd} = 1$, $t_{pp} = 0.5$, $\Delta = 3$, $U_d = 8$, $U_p = 3$, and $U_{pd} = 1$, which are almost in proportion to the values $t_{pd} = 1.3$ eV, $t_{pp} = 0.65$ eV, $\Delta = 3.6$ eV, $U_d = 10.5$ eV, $U_p = 4$ eV, and $U_{pd} = 1.2$ eV derived from the constrained-density-functional approach.[25] Dimensionless electron-lattice coupling strengths are defined by $\lambda_\alpha = \alpha^2/(Kt_{pd})$ and $\lambda_\beta = \beta^2/(Kt_{pd})$. Hereafter we denote by the "reference parameter set" the electronic parameters as above and $\lambda_\alpha = \lambda_\beta = 0$. It is easily shown that, within the present mean-field theory, two parameter sets differing only by $\bar{g}^k_{ij} = s\bar{g'}^k_{ij}$ ($\alpha = s\alpha'$, $\beta = s\beta'$) and $K_{kl} = s^2K'_{kl}$ (thus $\lambda_\alpha = \lambda'_\alpha$, $\lambda_\beta = \lambda'_\beta$, s a real number) give the same HF configuration for charge and spin densities and the lattice displacements related by $\langle u_k\rangle = s^{-1}\langle u'_k\rangle$. When we study lattice fluctuation (in the RPA), we use $K = 32$, which gives a dispersionless bare O phonon frequency of 104 meV (840 cm^{-1}) if this value is interpreted as $K = 32 \times 1.3$ eV/Å^{-2}. This value is also consistent with "local-density-approximation (LDA)+U" calculations[13] as we will show later (Sec. III F).

In addition, we use other parameter sets in which selected parameter values are varied from the reference parameter set: (i) $U_d = 10$ is used in addition to $U_d = 8$ to study the effect of varying U_d. (ii) U_{pd} is taken in the range $1 \leq U_{pd} \leq 3$ to study the effect of varying U_{pd}. (iii) Either λ_α or λ_β is set to finite values to study the effect of intersite and intrasite electron-lattice couplings. To show that this effect can overcome the effect of U_d *locally*, we use $U_d = 10$ in addition to $U_d = 8$. To show the lattice effect on the phase separation, we vary U_{pd} ($1 \leq U_{pd} \leq 3$). When U_d or U_{pd} is varied in the above cases, Δ is also varied as will be explained in Sec. III B.

III. MEAN-FIELD STATES

Our analysis proceeds in two steps. First mean-field states are obtained and next quantum fluctuations are added to them. For obtaining mean-field states, the lattice displacements u_k are divided into a classical static component $\langle u_k\rangle$ and a quantum-mechanical fluctuating component $\hat{u}_k$,

$$u_k = \langle u_k\rangle + \hat{u}_k \quad . \tag{4}$$

Self-consistency conditions for the electronic part (the HF equation) and the lattice part are derived in Appendix A. The HF equation is

$$\sum_{j(\neq i)} t_{ij}(\{\langle u_k\rangle\})\phi_\lambda(j\sigma) + e_i(\{\langle u_k\rangle\})\phi_\lambda(i\sigma)$$

$$+\left(U_i\langle c^\dagger_{i\bar\sigma}c_{i\bar\sigma}\rangle + \sum_{j(\neq i),\sigma'} U_{ij}\langle c^\dagger_{j\sigma'}c_{j\sigma'}\rangle\right)\phi_\lambda(i\sigma)$$

$$-U_i\langle c^\dagger_{i\bar\sigma}c_{i\sigma}\rangle\phi_\lambda(i\bar\sigma) - \sum_{j(\neq i),\sigma'} U_{ij}\langle c^\dagger_{j\sigma'}c_{i\sigma}\rangle\phi_\lambda(j\sigma')$$

$$= \epsilon_\lambda\phi_\lambda(i\sigma), \quad (5)$$

with self-consistently determined one-body densities,

$$\langle c^\dagger_{i\sigma}c_{j\sigma'}\rangle = \sum_{\lambda\in\mathrm{occ}} \phi^*_\lambda(i\sigma)\phi_\lambda(j\sigma') \quad . \quad (6)$$

Solution of the HF equation gives the HF energy levels ϵ_λ and their wave functions $\phi_\lambda(i\sigma)$. Self-consistency conditions for the lattice displacements are

$$\sum_{i,j,\sigma} \bar g^k_{ij}\langle c^\dagger_{i\sigma}c_{j\sigma}\rangle + \sum_l K_{kl}\langle u_l\rangle = 0 \quad , \quad (7)$$

which holds in the adiabatic ($M_l \to \infty$) limit. The kinetic part of the lattice is incorporated later (see Secs. IV and V) with particle-hole excitations in the RPA analysis.

Mean-field states are obtained by solving the above HF equation with self-consistency conditions for on-site and nearest-neighbor charge and spin densities as well as lattice displacements, without assumption on the form of these quantities.[21,22] Calculations were made for systems of 6×6 CuO_2 unit cells with periodic boundary condition. The stability of mean-field states is investigated by adding small random numbers to the self-consistent charge-spin densities and lattice displacements at every site after a convergence. A similar HF study for a 2D two-band Hubbard model (with t_{pd}, Δ, U_d terms and no electron-lattice coupling) has reported charged magnetic domain walls for doping of ten holes in 9×10 and 10×10 systems.[20]

A. Doping states in the LDA parameter set

First we show the doping state in the reference parameter set ($t_{pd} = 1$, $t_{pp} = 0.5$, $\Delta = 3$, $U_d = 8$, $U_p = 3$, $U_{pd} = 1$, and $\lambda_\alpha = \lambda_\beta = 0$). Each added hole is localized primarily on a single Cu site and four surrounding O sites (Fig. 1). The spin density at this Cu site is flipped so that a small ferromagnetic polaron is formed. The spin densities at the four O sites are small and in the opposite direction to the central Cu spin. Five HF eigenstates appear inside the charge-transfer gap per added hole. [In all the HF energy levels in the figures below, the center of the charge-transfer gap in the stoichiometric case has been set to zero. Only the lowest third of the HF energy levels (i.e., near the charge-transfer gap) are plotted in increasing order except in Fig. 2 where the dispersion relation in the stoichiometric AF state is shown.] The HF wave functions associated with the gap states are spatially localized. Note that all of these gap states are occupied by holes. Among the five, two appear deep within the gap and three are near the valence band (the lower Hubbard band in a hole description).

The highest occupied HF eigenstate corresponds to a symmetric O state formed by the four O states and has small weight on the Cu site. The second highest mainly corresponds to the central Cu state with opposite spin to the highest one. This state is thus regarded as a HF analog of the Zhang-Rice singlet state,[26] where the central Cu orbital and the symmetric orbital made from the four O orbitals constitute a singlet. Since a HF state is a single Slater determinant, it cannot describe such a Heitler-London-like singlet. However, if quantum fluctuations are fully taken into account, the above HF state would be superposed with a similar state in which the spin directions at the central Cu site and the four O sites are reversed. The three remaining HF eigenstates near the valence band are made from four Cu states around the central Cu site.

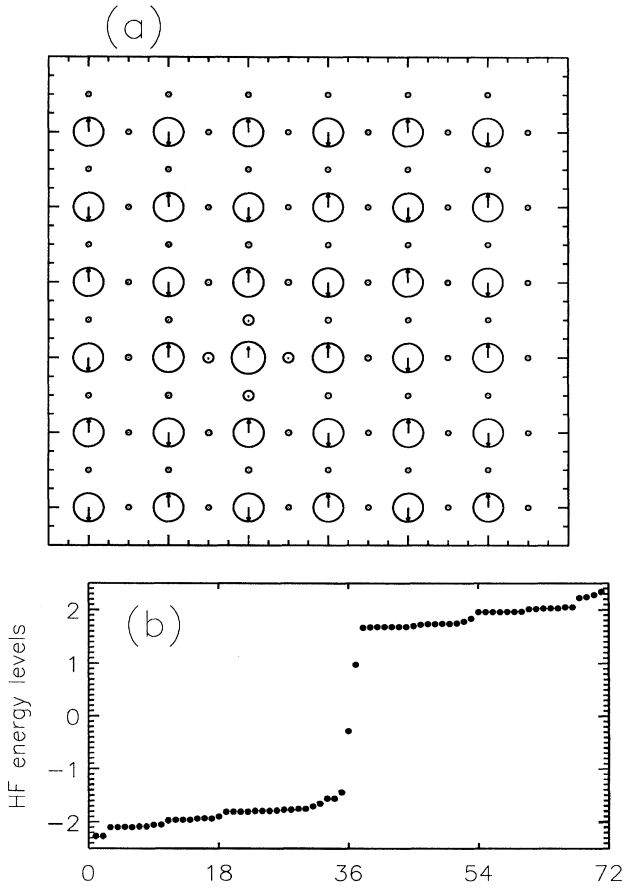

FIG. 1. (a) Spin and charge densities and (b) HF energy levels around the gap for the one-hole-doped system with a small ferromagnetic polaron. Parameters are $t_{pd} = 1$, $t_{pp} = 0.5$, $\Delta = 3$, $U_d = 8$, $U_p = 3$, $U_{pd} = 1$, and $\lambda_\alpha = \lambda_\beta = 0$. Spin and charge densities are represented by arrows and radii of the circles, respectively. The arrows are normalized so as to touch the circle if completely polarized. Big (small) circles are for Cu (O) sites. Energy levels are relative to the gap center in the stoichiometric case.

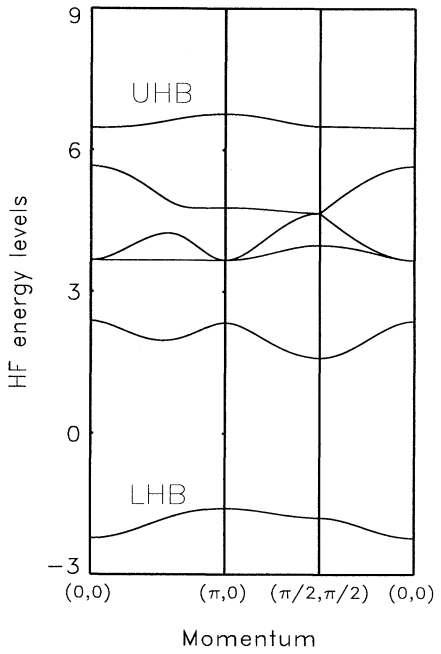

FIG. 2. Dispersion relation of HF energy levels in the stoichiometric AF state. Parameters are $t_{pd} = 1$, $t_{pp} = 0.5$, $\Delta = 3$, $U_d = 8$, $U_p = 3$, and $U_{pd} = 1$.

B. Effect of varying parameters on the stoichiometric state

Before investigating the effect of changing various model parameters on doping states, we study how the stoichiometric state (one hole per CuO_2 unit) changes with different parameter values. Around the reference parameter set, the stoichiometric state accommodates holes mainly at Cu sites. Because of the strong on-site repulsion at Cu sites, U_d, double occupancy is suppressed there and the spin density is aligned antiferromagnetically. This causes period doubling and the Brillouin zone is halved. Thus six bands are formed (Fig. 2), the lowest of which is occupied by holes and the others are unoccupied. The lowest band can be termed the lower Hubbard band (LHB) in a hole description (or the upper Hubbard band in an electron description). Among the unoccupied five bands, one lies beyond the others, due to strong U_d, and corresponds to the upper Hubbard band (UHB). Both Hubbard bands mainly consist of Cu states, whereas the remaining four are mainly constructed from O states so that they are termed O bands. When the direct O-O hopping t_{pp} is absent, two of them form a dispersionless nonbonding O band and they are distinguished from the other bonding O bands. The charge-transfer gap denotes the energy difference between the lowest unoccupied level (in the O band) and the highest occupied level (in the lower Hubbard band).

Since hole-doping states are our main interest, we first focus on the lowest unoccupied O band and study how it changes with different parameter values. It will be shown later that the momentum of the lowest unoccupied state is an important factor for determining doping states. In the reference parameter set, the momentum of the lowest unoccupied state is $(\pi/2, \pi/2)$ in terms of the original (nonmagnetic) Brillouin zone. The nearest-neighbor Cu-O hopping t_{pd} is always set to unity. When t_{pp} is increased, the lowest O band is widened, but the momentum of the lowest unoccupied state is unchanged. It is similar to the case when the site-energy difference Δ is decreased. When Δ is increased, the momentum shifts from $(\pi/2, \pi/2)$ to (0, 0) around $\Delta = 6$ (with the other parameters kept fixed at the values of the reference parameter set). The other electronic parameters U_d, U_p, and U_{pd}, determining repulsion strengths, have little effect on the shape of the lowest O band.

When U_d or U_{pd} is varied later, we will also change Δ to keep the renormalized site-energy difference $\Delta_{\rm ren} = \Delta - \frac{U_d}{2} n_d + \frac{U_p}{2} n_p + 2U_{pd}(n_d - 2n_p)$ nearly a constant value in the stoichiometric AF state (n_d and n_p are hole densities at Cu and O sites, respectively, with $n_d + 2n_p = 1$). As U_d increases with U_{pd} unchanged, n_d approaches to 1 and n_p to 0, so that $\Delta_{\rm ren}$ is almost a constant value when $\Delta - \frac{U_d}{2}$ is kept fixed. Indeed for $U_d = 8$, 10, 12 with $\Delta - \frac{U_d}{2} = -1$, $\Delta_{\rm ren} = 1.2$, 1.3, 1.3, $m_{\rm Cu}$ (staggered magnetization at Cu site) = 0.74, 0.82, 0.88, and the (indirect) charge-transfer gap = 3.2, 4.4, 5.6, respectively. When U_d is further increased ($U_d > 13$) with increasing Δ, the momentum of the lowest unoccupied state becomes (0, 0) due to the large Δ as mentioned above. It will be shown later that an intermediate-size (not small) ferromagnetic polaron is obtained for these large U_d values. We note that, in this very large U_d and Δ regime, the shape of the lowest O band, including its width and the momentum of the lowest unoccupied state, is almost the same as that of a strong-coupling expansion[27] around the classical Néel state.

When U_{pd} is increased with U_d unchanged, n_d deviates from 1 and n_p from 0, so that $\Delta_{\rm ren}$ deviates from its strong-coupling value $\Delta - \frac{U_d}{2} + 2U_{pd}$. Indeed for $U_{pd} = 0$, 1, 2 with $\Delta + 2U_{pd} = 5$, $\Delta_{\rm ren} = 1.7$, 1.2, −0.7. Instead we change Δ with $\Delta + \frac{U_{pd}}{2} = 3.5$ so that, for $U_{pd} = 0$, 1, 2, $\Delta_{\rm ren} = 0.7$, 1.2, 1.7, $m_{\rm Cu} = 0.73$, 0.74, 0.75, and the charge-transfer gap = 2.6, 3.2, 3.8, respectively. We note that, when U_{pd} is further increased with $\Delta + \frac{U_{pd}}{2} = 3.5$, $\Delta_{\rm ren}$ becomes negative around $U_{pd} = 2.7$ *if* a paramagnetic state is assumed. ($\Delta_{\rm ren}$ is always positive in the AF state.) It will be shown later that phase separation into Cu- and O-hole-rich regions occur roughly for U_{pd} larger than this value. In summary, when U_d or U_{pd} is varied, we used $\Delta - \frac{U_d}{2} + \frac{U_{pd}}{2} = -0.5$ so as to have $1 \lesssim \Delta_{\rm ren} \lesssim 2$.

C. Doping states with different U_d values

When U_d is large ($U_d = 10$, $\Delta = 4$), the small ferromagnetic polaron in Sec. III A becomes metastable, and a new state acquires lower total energy within the HF approximation. In the latter state, each added hole is extended to about four Cu sites and their surrounding O sites (Fig. 3). The spin densities at these Cu sites are almost aligned in the same direction so that this con-

figuration is termed an intermediate-size ferromagnetic polaron. Note that the Cu spins inside the polaron are perpendicular to the background AF Cu spins. The O sites inside the polaron have very small spin densities. Around the polaron, the Cu spins have small ferromagnetic components decaying slowly with distance. Seven localized HF eigenstates appear inside the gap, of which the two highest states lie near the O band and are unoccupied, the next highest state also lies near the O band but is occupied, and the other four lie near the lower Hubbard band and are occupied. The two unoccupied HF eigenstates mainly correspond to O states around the polaron. The highest occupied HF eigenstate corresponds to a symmetric O state formed by the four O states bridging the four Cu sites and has small weight on these Cu sites. The four remaining HF eigenstates near the lower Hubbard band correspond to the four Cu states. Reflecting a more extended texture than the small polaron, all of these gap energy levels are located near the band edges.

The effect of U_d can be understood from the dispersion relation of HF energy levels in the undoped case. As U_d increases, the momentum of the lowest unoccupied state changes from $(\pi/2, \pi/2)$ to $(0, 0)$ at $12 < U_d < 13$. When a hole is added to the undoped system, it first occupies this state before relaxation. After doping, HF eigenstates are relaxed, inhomogeneously distorting charge and spin densities and lowering total energy. For the larger U_d case, the highest occupied HF eigenstate is relaxed from the state with momentum (0, 0), which is compatible with the ferromagnetic component of the intermediate-size polaron. Thus, after relaxation, the polaron would be more extended because the added hole would be less affected by the more compatible background AF Cu spins. The actual transition from the small to intermediate-size ferromagnetic polaron occurs at $8 < U_d < 10$. The intermediate-size polaron is unstable for the reference parameter set ($U_d = 8$), while the small polaron becomes metastable for $U_d = 10$, where tunneling (or dynamic oscillation) between the two polarons can be anticipated but is beyond our mean-field level calculations.

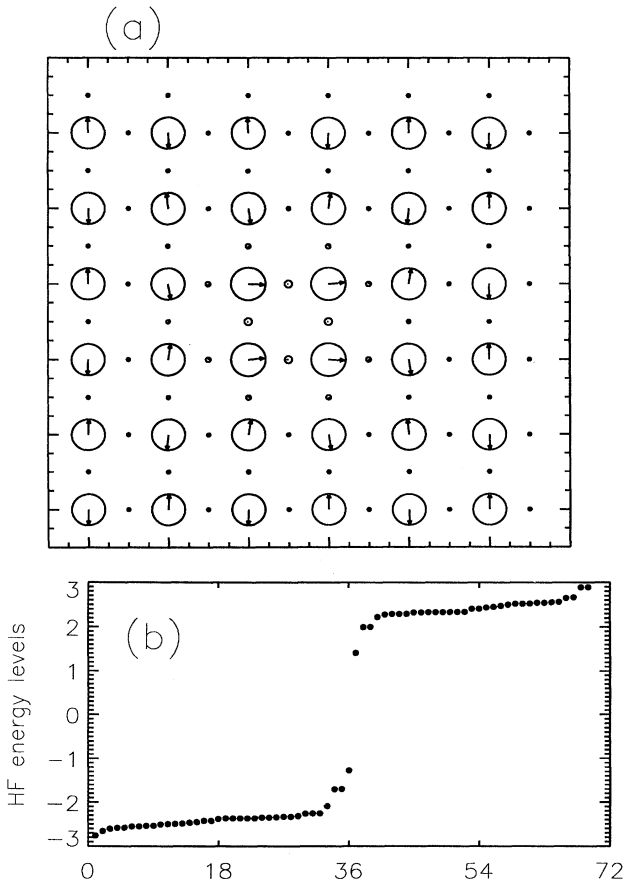

FIG. 3. (a) Spin and charge densities and (b) HF energy levels around the gap for the one-hole-doped system with an intermediate-size ferromagnetic polaron. Parameters are $t_{pd} = 1$, $t_{pp} = 0.5$, $\Delta = 4$, $U_d = 10$, $U_p = 3$, $U_{pd} = 1$, and $\lambda_\alpha = \lambda_\beta = 0$. The symbols are as in Fig. 1.

We note that, in the 2D one-band Holstein-Hubbard model, Zhong and Schüttler have shown a delocalized phase at very small electron-lattice coupling and a polaronic phase at moderate coupling, and suggested local tunneling between the delocalized and self-localized configurations near the boundary of the two phases.[7]

D. Doping states with different U_{pd} values

Here we add six holes to the 6×6 system to focus on how the system is separated into Cu- and O-hole-rich regions as a function of U_{pd}. For example, for $U_{pd} = 3$ and $\Delta = 2$ where the phase separation occurs, the two regions are clearly seen, divided by a "boundary," when six holes are added; but only the boundary region is seen in a Cu-hole-rich background when four holes are added. (Thus we conclude that four added holes are not enough to form an O-hole-rich region in this case.)

As U_{pd} increases, for $U_{pd} \leq 2.4$ the six holes remain isolated small ferromagnetic polarons as in Sec. III A; for $2.6 \leq U_{pd} \leq 2.8$ they clump to form a rectangular "cluster boundary" dividing the two degenerate Cu AF phases (Fig. 4); and finally for $2.9 \leq U_{pd}$ the cluster boundary and the interior Cu AF phase are replaced by an O-hole-rich phase separated from the Cu-hole-rich background phase (Fig. 5). More precisely, some portion of the exterior Cu AF phase is also replaced by the O-hole-rich phase. This is because the number of added holes is roughly proportional to the length of the cluster boundary before the phase separation, while it is nearly proportional to the area of the O-hole-rich region in the phase-separated state. This phase-separated state has been suggested and discussed in exact-diagonalization studies at strong coupling,[10] and it is a real-space manifestation of charge fluctuation softening tendencies with U_{pd} found in weak-coupling RPA approaches.[11] The phase separation and clumping we obtained here are qualitatively consistent with the results obtained in 1D and 2D spinless fermion models.[12] Note that the stoichiometric state re-

mains the pure Cu AF state at least for $U_{pd} \leq 4$. (For $U_{pd} \simeq 5$, this is no longer stable.)

In the cluster-boundary state ($U_{pd} = 2.6$, $\Delta = 2.2$), the added holes are on the boundary and in the interior Cu AF phase (Fig. 4). The Cu-hole densities are slightly smaller in the interior phase than the exterior phase. Substantial O-hole densities are distributed in the interior phase and on the boundary. Thus this state can be regarded as a precursor of the phase separation, although it is difficult to distinguish the cluster-boundary state from the phase-separated state for small systems. Twelve (twice the number of added holes) HF eigenstates deep within the charge-transfer gap mainly correspond to the boundary Cu states substantially mixed with nearby O states. There are other localized HF eigenstates near the lower Hubbard band, which correspond to an interior Cu state or exterior Cu states localized near the boundary.

In the phase-separated state ($U_{pd} = 3$, $\Delta = 2$), the Cu and O spin densities are aligned antiferromagnetically in the respective Cu- and O-hole-rich regions (Fig. 5). The AF Cu spins and the AF O spins are nearly perpendicular to each other, so that on the boundary both spin densities are frustrated and deviated from the respective perfect AF alignments. Intragap HF eigenstates appear, forming a rather wide band of mainly O states in the O-hole-rich region. The width of this band is due to the direct hopping between neighboring O sites (t_{pp}) and small O-site repulsion (U_p). There are other localized HF eigenstates near the lowest unoccupied O band, which also correspond to O states in the O-hole-rich region. The states in the lower Hubbard band correspond to Cu states in the Cu-hole-rich region.

E. Lattice effects on the stoichiometric state

Electron-lattice coupling modifies the above doping states. Before investigating the doping states, we mention how the stoichiometric state is changed with intersite

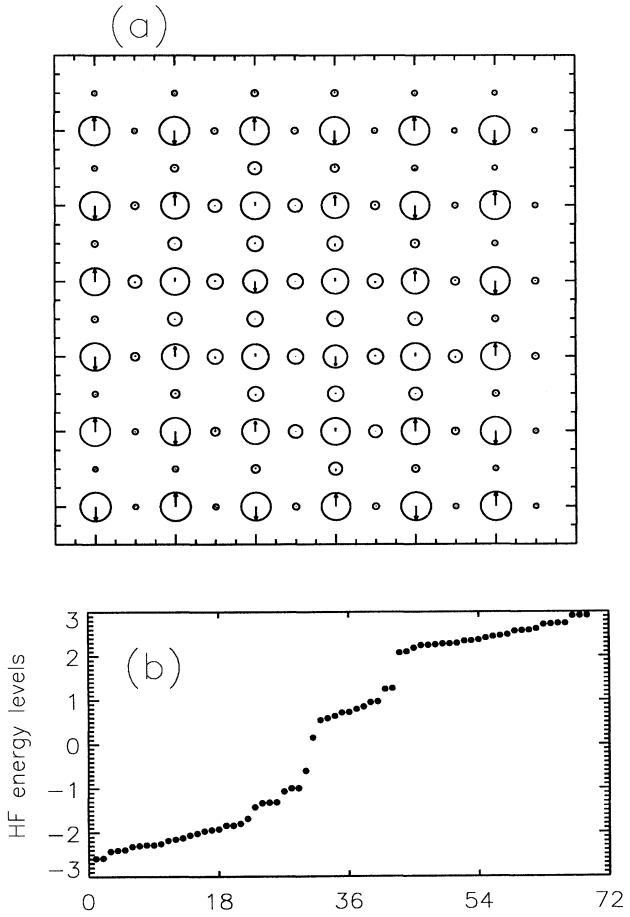

FIG. 4. (a) Spin and charge densities and (b) HF energy levels around the gap for the six-hole-doped system with a rectangular cluster boundary. Parameters are $t_{pd} = 1$, $t_{pp} = 0.5$, $\Delta = 2.2$, $U_d = 8$, $U_p = 3$, $U_{pd} = 2.6$, and $\lambda_\alpha = \lambda_\beta = 0$. The symbols are as in Fig. 1.

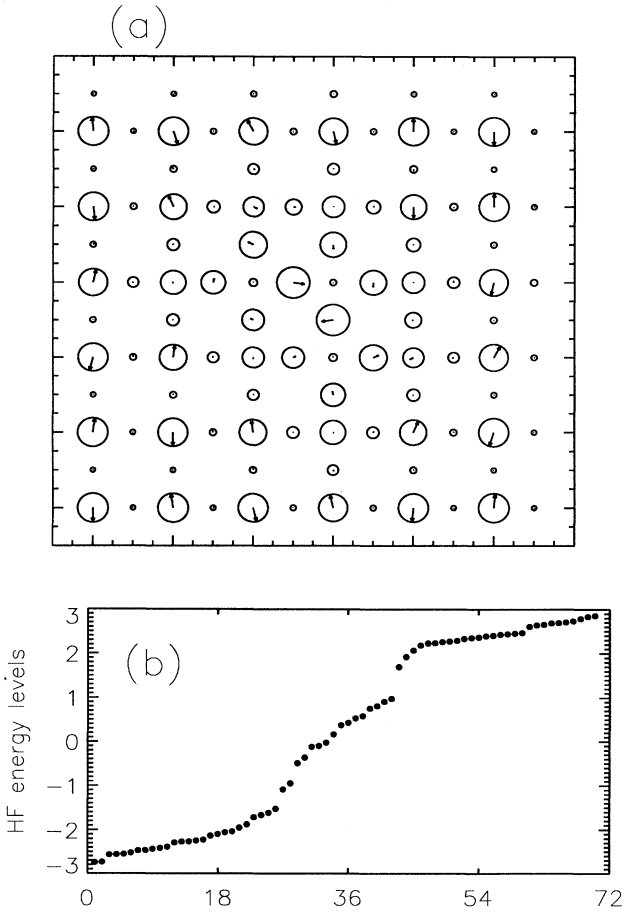

FIG. 5. (a) Spin and charge densities and (b) HF energy levels around the gap for the six-hole-doped system with phase separation. Parameters are $t_{pd} = 1$, $t_{pp} = 0.5$, $\Delta = 2$, $U_d = 8$, $U_p = 3$, $U_{pd} = 3$, and $\lambda_\alpha = \lambda_\beta = 0$. The symbols are as in Fig. 1.

(λ_α) and intrasite (λ_β) electron-lattice couplings. Note that λ_α and λ_β represent the electron-lattice coupling strengths through modifications of the nearest-neighbor Cu-O hopping and the Cu-site energy, respectively, by planar O-atom displacements. There is no lattice distortion in the stoichiometric state until a critical strength ($\lambda_{\alpha c}$ or $\lambda_{\beta c}$) is reached, within the present mean-field approach, so that the HF configuration is unchanged, including charge and spin densities, HF energy levels and wave functions, and the total energy.

For $\lambda_\alpha > \lambda_{\alpha c}$, the stoichiometric system becomes a bond-order-wave (BOW) state, in which O atoms are displaced periodically to form alternating bond-charge densities, $\sum_\sigma \langle c^\dagger_{i\sigma} c_{j\sigma} \rangle$ (i and j are neighboring Cu and O sites). The O-atom lattice configuration can be regarded as "breathing" modes which are frozen quite asymmetrically: Only one of the four O atoms around each Cu site is significantly displaced. The bond-charge density is enhanced on the corresponding short bonds. Spin densities vanish everywhere. The critical strength is $\lambda_{\alpha c} \simeq 1.3$ for the otherwise reference parameter set; and $\lambda_{\alpha c} \simeq 1.7$ for $U_d = 10$, $\Delta = 4$, and otherwise the same as the reference parameter set.

When we take small U_d values not directly related to the copper oxides, several different phases are obtained at stoichiometry.[18] For strong intersite electron-lattice coupling ($\lambda_\alpha = 2$), we found, with increasing U_d, a charge-density-wave (CDW) state with symmetric breathing modes frozen, the BOW state, a mixed state of spin-Peierls bonds and antiferromagnetic spins, a spin Peierls state, and the AF state. This variety is caused by competitions between magnetism and covalency of different relative strengths. These phases and corresponding doping states in a wider parameter space are reported elsewhere.[18]

For $\lambda_\beta > \lambda_{\beta c}$, the system becomes a CDW state, where O-atom breathing modes are frozen. Namely, around each Cu site, the four surrounding O atoms are symmetrically displaced either from or toward it to have alternating Cu-hole densities. Spin densities vanish everywhere. The critical strength is $\lambda_{\beta c} \simeq 1.0$ for the otherwise reference parameter set; and $\lambda_{\beta c} \simeq 1.2$ for $U_d = 10$, $\Delta = 4$, and otherwise the same as the reference parameter set.

The above CDW states are similar to the disproportionated state observed in the bismuthates, although the latter are 3D materials and have small U_d.[6]

F. Lattice effects on polaron states

Now we investigate how the intersite electron-lattice coupling (λ_α) modifies the small polaron in the reference parameter set. For $\lambda_\alpha = 1.125$, the four O atoms in the small polaron are displaced toward the central Cu site and suppress the spin densities at these five sites (Fig. 6). Thus this configuration is termed a small nonmagnetic polaron. The local lattice distortion enhances the hopping integral on the four Cu-O bonds and makes a local antibonding orbital, consisting of the central Cu state and the symmetric O state formed by the four surrounding O states, well split from the bonding orbital.

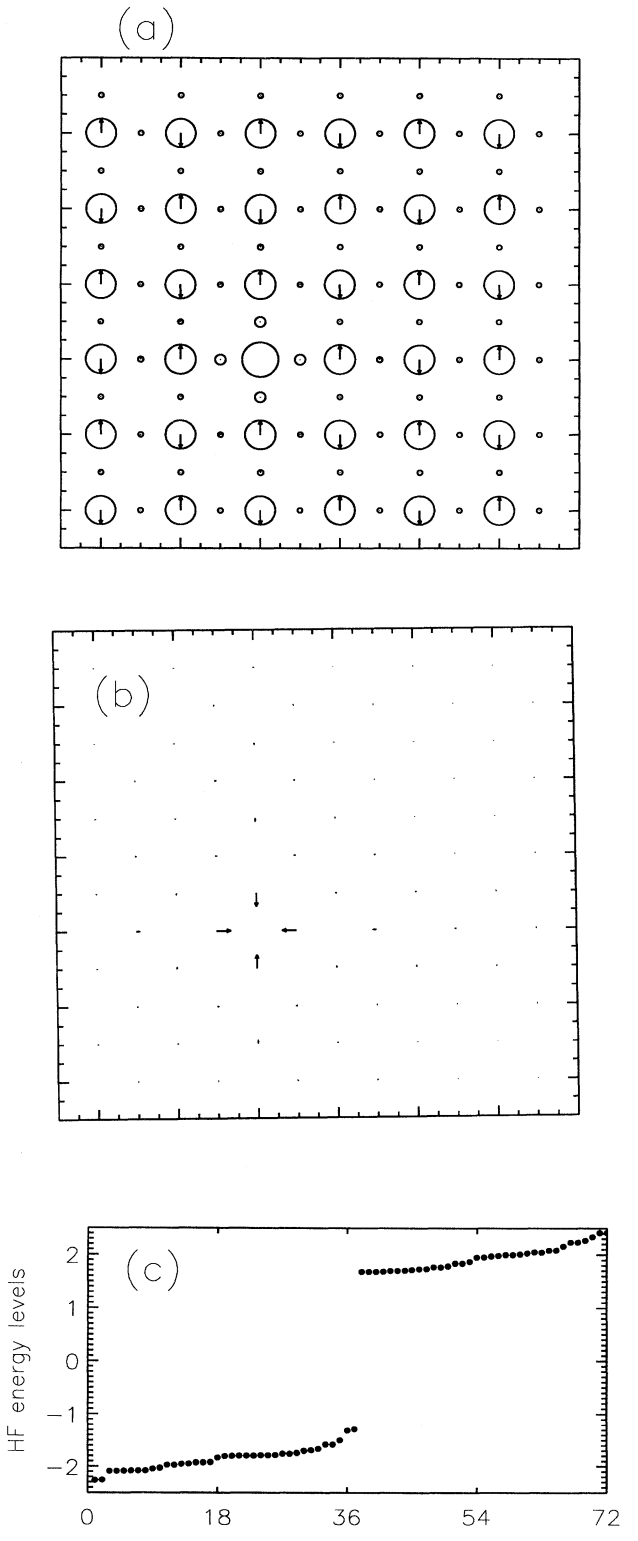

FIG. 6. (a) Spin and charge densities, (b) O-atom displacements, and (c) HF energy levels around the gap for the one-hole-doped system with a small nonmagnetic polaron. Parameters are $t_{pd} = 1$, $t_{pp} = 0.5$, $\Delta = 3$, $U_d = 8$, $U_p = 3$, $U_{pd} = 1$, $\lambda_\alpha = 1.125$, and $\lambda_\beta = 0$. The symbols are as in Fig. 1.

(The antibonding orbital is lower than the bonding orbital in a hole description due to the reversed sign of the hopping integral.) This local antibonding orbital, lying near the lower Hubbard band, is the highest occupied HF eigenstate. Both spin states occupy this antibonding orbital to cancel spin densities there. There are three other local HF eigenstates. These lie close to the lower Hubbard band and are formed from four Cu states around the central Cu site.

This local quenching of a magnetic moment on the central Cu site and the accompanying local lattice distortion reinforce each other [Fig. 7(a)]. To appreciate this phenomenon, suppose the magnetic moment on the central Cu site points up before turning on the intersite electron-lattice coupling. Once the magnetic moment is reduced, it raises the corresponding Cu-site energy for the up spin, which was originally in the lower Hubbard band, and it lowers that for down spin, which was in the upper Hubbard band. The raised local Cu state [up spin, dashed line in Fig. 7(b)] is more mixed with the surrounding O states so as to generate more weight on the four O sites. The symmetric O state [down spin, solid line in Fig. 7(b)] is more mixed with the central Cu state to produce more weight on this Cu site. This local mixing further reduces the magnetic moment on the central Cu site. Thus the above mechanism indeed feeds back positively.

The intersite electron-lattice coupling (λ_α) enhances this mechanism by locally distorting the O lattice,

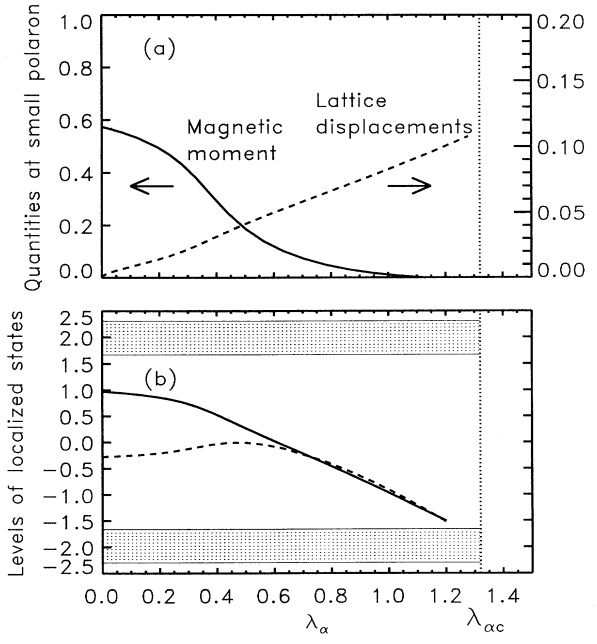

FIG. 7. (a) Magnetic moment on the central Cu site and ratio of the displacement of the surrounding O atoms to the Cu-O distance (1.89 Å) and (b) gap energy levels, for the small-polaron state as functions of λ_α. Other energy levels in the gap close to the bands (shaded areas) are not shown. Parameters are $t_{pd} = 1$, $t_{pp} = 0.5$, $\Delta = 3$, $U_d = 8$, $U_p = 3$, $U_{pd} = 1$, $\lambda_\beta = 0$, and $K = 32t_{pd}/\text{Å}^2$.

strengthening the Cu-O hopping integral, and increasing the local mixing. Note that the position of an O atom is determined by the difference of bond-charge densities between the neighboring Cu-O bonds, as is easily seen in Eq. (7). The bond-charge densities on the central Cu-O bonds are larger than those on the other Cu-O bonds due to the local mixing so that the four O atoms are forced toward the central Cu site, lowering the total energy. This in turn further increases the local mixing, enlarging the difference of the bond-charge densities and further shifting the O atoms. Thus it enhances the feedback mechanism. Finally the two gap states become nearly degenerate to form the local antibonding orbital, suppressing the spin densities in the small polaron (Fig. 6). This can be viewed as a rapid crossover from a Heitler-London-like state corresponding to the Zhang-Rice singlet to a highly covalent molecular state, although a Heitler-London-like singlet is not precisely described by the HF approximation. Note that this rapid crossover occurs substantially *below* $\lambda_{\alpha c}$ due to the feedback mechanism. As λ_α increases in the covalent molecular regime, the antibonding orbital is lowered by the increasing local covalency.

To deduce the strength of the intersite electron-lattice coupling, we can compare the above result with the recently introduced "LDA+U" method,[13] where the LDA single-particle potential is augmented with an orbital- and spin-dependent Hartree potential for the Hubbard (U) and exchange (J) interactions and applied to La_2CuO_4 and $La_{1.75}Sr_{0.25}CuO_4$ with a 2×2 supercell. Anisimov *et al.* have found, for the stoichiometric case, that a Cu magnetic moment, a charge-transfer gap, and the breathing-mode phonon frequency compare favorably with experiments. They have also found, for the doped case, that (i) without allowing lattice relaxation, a small ferromagnetic polaron exists with gap states similar to those in Fig. 7(b); (ii) with the four in-plane O atoms around a certain Cu site displaced along the Cu-O bonds, the energy is at minimum for a 2% contraction of the Cu-O bonds, the transfer integral for the short Cu-O bonds is increased, the O-like gap state is shifted further into the gap, and the magnetic moment on the central Cu site is reduced; and (iii) with two apical O atoms (not considered in our model) above and below a certain Cu site displaced along the bonds, a metastable anti-Jahn-Teller polaron exists *if* the additional hole is constrained to have the $3z^2 - r^2$ symmetry. Their results for the cases (i) and (ii) are compatible with ours.

In the case (i) above, the magnetic moments on the central Cu site and the next-nearest Cu site (longest-distance in the 2×2 supercell) are -0.55 and 0.72, respectively, while our corresponding results for the reference parameter set are -0.57 and 0.74, respectively. In the case (ii) above, they are -0.43 and 0.73, respectively, while our results for $\lambda_\alpha = 0.28$ and the otherwise reference parameter set are -0.43 and 0.74, respectively. We can thus obtain a value of λ_α, which is compatible with the LDA+U result, using the sensitivity of the small polaron to the intersite electron-lattice coupling. As shown later, the magnetic moments are insensitive to change of λ_β so that it is hard to estimate a value of λ_β appropriate for the material. Note that the HF configura-

tion, including the magnetic moments, does not change if α and K are varied but $\lambda_\alpha = \alpha^2/(Kt_{pd})$ is kept fixed. (See the previous section or the last part of Appendix I for more detail.) To obtain a 2% contraction of the Cu-O bonds, we need $K = 32t_{pd}/\text{Å}^2 \simeq 42$ eV/Å^2, which gives $\alpha = (\lambda_\alpha K t_{pd})^{\frac{1}{2}} = 3t_{pd}/\text{Å} \simeq 4$ eV/Å. These parameter values give the in-plane stretching IR-active phonon frequency 760 cm^{-1} (when lattice fluctuation is incorporated with particle-hole excitations in the RPA analysis below), which is comparable with the experimentally observed value 706 cm^{-1}.[16]

Next we study how the intrasite electron-lattice coupling (λ_β) modifies the small polaron in the reference parameter set. In this case, the four O atoms in the small polaron are displaced toward the central Cu site. However, the local lattice distortion is much smaller than the case of the same value for λ_α and $\lambda_\beta = 0$ [Fig. 8(a)]. It only lowers the Cu-site energy at the center of the small polaron, but hardly affects the Cu magnetic moment. The gap states are almost unchanged [Fig. 8(b)]. In contrast to the intersite electron-lattice coupling (λ_α), the doping state is insensitive to λ_β until it approaches very close to the critical strength $\lambda_{\beta c}$. This is because the system can gain energy only by increasing the hole density and consequently the double occupancy at the central Cu site by the four O atoms approaching this Cu site. Thus this coupling directly competes against the strong on-site repulsion U_d at Cu sites. It contrasts with λ_α, which can gain energy by increasing local covalency. Note that for finite λ_α the position of an O atom was determined from the difference of bond-charge densities between the neighboring Cu-O bonds; for finite λ_β it is determined by the difference of hole densities between the neighboring Cu sites, as is easily seen in Eq. (7). The hole density on the central Cu site is slightly larger than that on the four neighboring Cu sites so that the four O atoms are forced slightly toward the central Cu site. This should further increase the difference of the hole densities and further shift the O atoms. But this happens only slightly, being inhibited by the strong on-site repulsion U_d at Cu sites.

Finally, we look at how the electron-lattice couplings modify the intermediate-size polaron for $U_d = 10$, $\Delta = 4$, and the otherwise reference parameter set. The intermediate-size polaron is accompanied by slight lattice distortion on the boundary between the polaronic region and the AF background. As λ_α increases, it is stable for $0 \leq \lambda_\alpha \lesssim 0.4$, metastable for $0.4 \lesssim \lambda_\alpha \lesssim 0.5$, and unstable for $0.5 \lesssim \lambda_\alpha$ (Fig. 9). For $\lambda_\alpha \gtrsim 0.4$, the small polaron becomes stable, which is also accompanied by local lattice distortion as already described. As λ_α increases further, the rapid crossover from the Zhang-Rice regime to the covalent molecular regime occurs as reported in Figs. 1(a) and 1(b) of Ref. 9 for the $(U_d, \Delta)=(10,4)$ case, which is similar to Figs. 7(a) and 7(b) for the $(U_d, \Delta)=(8,3)$ case.

There is a difference between the $(U_d, \Delta)=(10,4)$ case [Figs. 1(a) and 1(b) of Ref. 9] and the $(U_d, \Delta)=(8,3)$ case [Figs. 7(a) and 7(b)] for $\lambda_\alpha \lesssim \lambda_{\alpha c}$. For the $(U_d, \Delta)=(10,4)$ case, when the nearly degenerate, local antibonding HF eigenstates approach the lower Hubbard band, they lose degeneracy between the up- and down-spin states. The down-spin local antibonding state [corresponding to the solid line in Fig. 7(b)], which was nearly the symmetric O state before turning on λ_α, is now nearly the central Cu state, so that it is compatible with other states in the lower Hubbard band. (Note that a down spin on the central Cu site in the stoichiometric AF state has been flipped into the up spin to form a small ferromagnetic polaron.) Meanwhile the up-spin local antibonding state [corresponding to the dashed line in Fig. 7(b)] is incompatible with the band due to the spin flipping, so that it is repelled from the band. For the $(U_d, \Delta)=(8,3)$ case, however, this lifting of the degeneracy between the up-

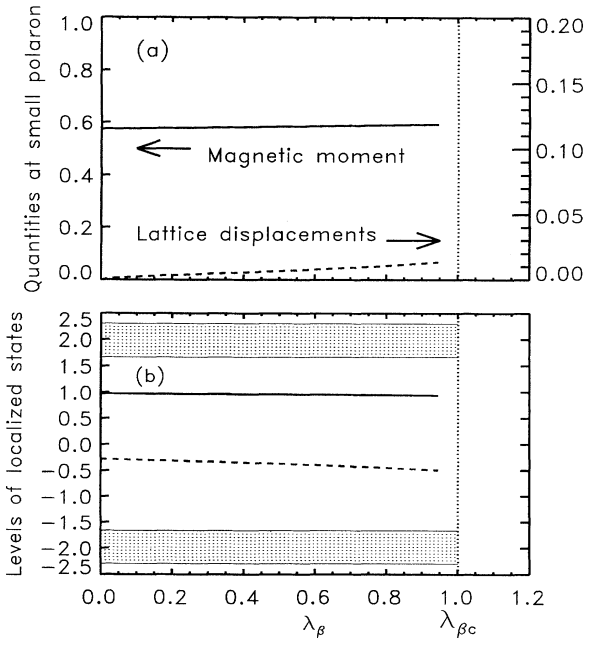

FIG. 8. (a) Magnetic moment on the central Cu site and ratio of the displacement of the surrounding O atoms to the Cu-O distance (1.89 Å) and (b) gap energy levels, for the small-polaron state as functions of λ_β. The symbols and the parameters are as in Fig. 7 except for finite λ_β and $\lambda_\alpha = 0$.

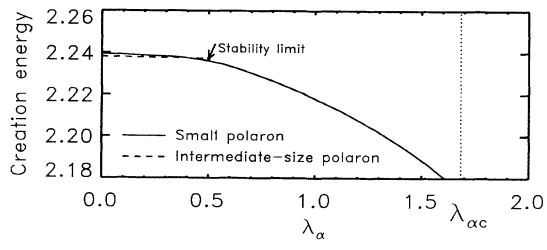

FIG. 9. Creation energy $\epsilon_1 = E^{N+1} - E^N - \bar{\mu}$ for the small- and intermediate-size-polaron states as a function of λ_α. E^{N+i} is the total energy with i added holes and $\bar{\mu}$ is the gap center in the stoichiometric case. Parameters are $t_{pd} = 1$, $t_{pp} = 0.5$, $\Delta = 4$, $U_d = 10$, $U_p = 3$, $U_{pd} = 1$, $\lambda_\beta = 0$, and $K = 32t_{pd}/\text{Å}^2$.

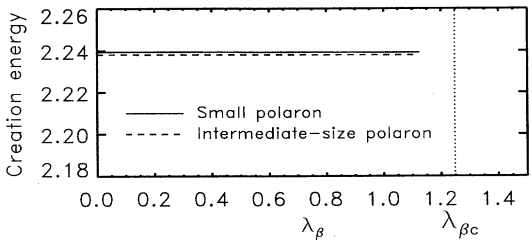

FIG. 10. Creation energy $\epsilon_1 = E^{N+1} - E^N - \bar{\mu}$ for the small- and intermediate-size-polaron states as a function of λ_β. The symbols and the parameters are as in Fig. 9 except for finite λ_β and $\lambda_\alpha = 0$.

and down-spin local antibonding HF eigenstates seems to be hidden by the smaller charge-transfer gap and the smaller value for $\lambda_{\alpha c}$.

The above transition from the intermediate-size polaron to the small polaron is another indication of the fact that the effect of the intersite electron-lattice coupling λ_α can overcome the effect of strong U_d *locally*. Meanwhile, the effect of λ_β is again very small. The intermediate-size polaron is largely insensitive to λ_β, which hardly changes its relative stability against the small polaron (Fig. 10). By increasing (U_d, Δ) from (8,3) to (10,4), the critical strengths $\lambda_{\alpha c}$ and $\lambda_{\beta c}$ and the value of λ_α for the crossover are rescaled to larger values nearly by the ratio of 10/8, showing a scaling property of these critical strengths with U_d/t_{pd} due to the competition between these electron-lattice couplings and the on-site repulsion.

G. Lattice effects on phase separation

Both the intersite (λ_α) and intrasite (λ_β) electron-lattice couplings tend to destabilize the cluster-boundary state (Fig. 4), found in the U_{pd} region between the isolated-small-polaron state and the phase-separated state. As a result, the electron-lattice couplings lower the critical strength of U_{pd} for the separation into Cu- and O-hole-rich phases ($U_{pd} \simeq 2.9$ for $\lambda_\alpha = \lambda_\beta = 0$; $U_{pd} \simeq 2.7$ for $\lambda_\alpha = 0.5$, $\lambda_\beta = 0$; $U_{pd} \simeq 2.5$ for $\lambda_\alpha = 0$, $\lambda_\beta = 0.8$).

For $\lambda_\alpha = 0.5$, $\lambda_\beta = 0$, and otherwise the same parameters as in Fig. 5, the O atoms are strongly displaced on the boundary between the Cu- and O-hole-rich regions (Fig. 11). They locally enhance the covalency on the Cu-O bonds to reduce the spin densities. Consequently, the spin frustration on the boundary (Fig. 5) is suppressed. The AF alignments in the Cu- and O-hole-rich regions are less affected by each other and deviate less. Thus the intersite electron-lattice coupling λ_α effectively isolates the O-hole-rich phase from the Cu-hole-rich phase. It increases the energy difference between the lowest unoccupied and highest occupied HF eigenstates so as to gain energy. The HF single-hole spectrum is otherwise similar to the case without electron-lattice coupling.

For $\lambda_\alpha = 0$, $\lambda_\beta = 0.8$, and otherwise the same parameters as in Fig. 5, a similar reduction of the spin frus-

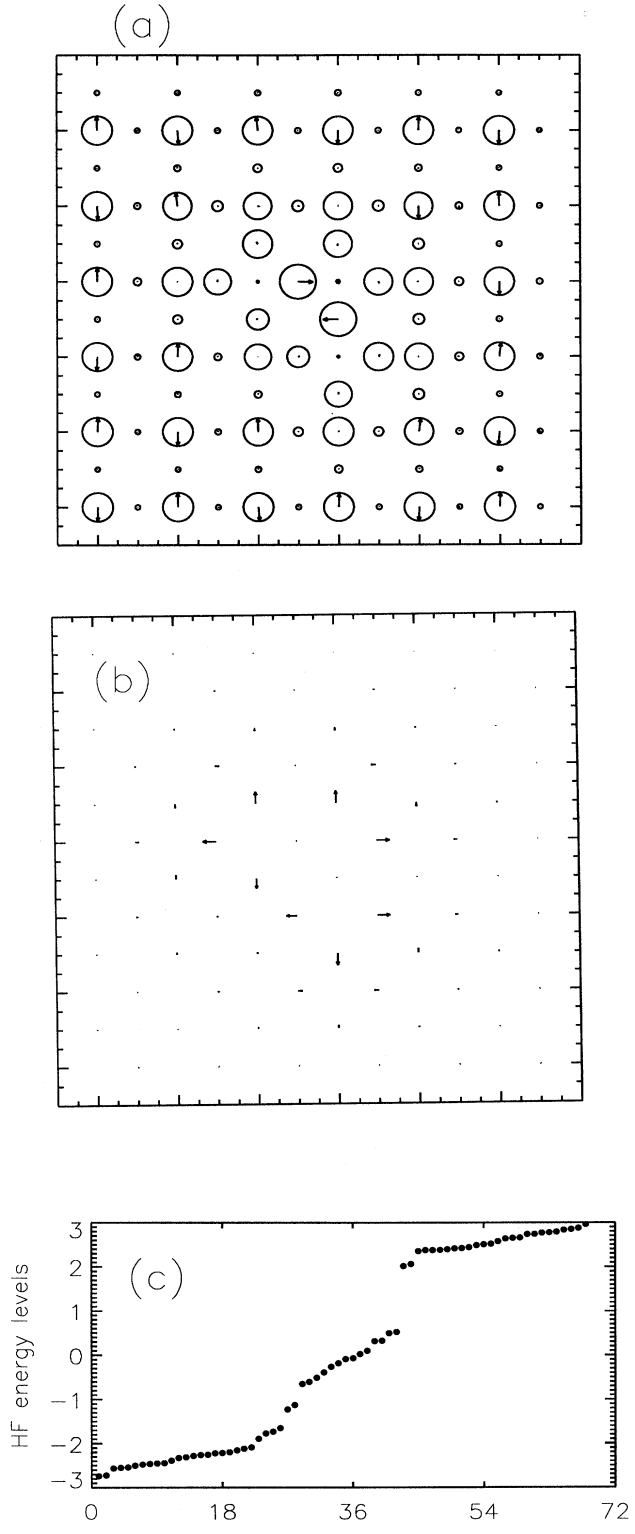

FIG. 11. (a) Spin and charge densities, (b) O-atom displacements, and (c) HF energy levels around the gap for the six-hole-doped system with phase separation. Note that lattice distortions on the boundary. Parameters are $t_{pd} = 1$, $t_{pp} = 0.5$, $\Delta = 2$, $U_d = 8$, $U_p = 3$, $U_{pd} = 3$, $\lambda_\alpha = 0.5$, and $\lambda_\beta = 0$. The symbols are as in Fig. 1.

tration occurs on the boundary. Here it is due to the local enhancement of the Cu-site double occupancy on the boundary. Therefore the reduction of the spin frustration is much smaller than that for $\lambda_\alpha = 0.5$, $\lambda_\beta = 0$, for the same reason as for the small and intermediate-size polarons. Again we see that *the intersite electron-lattice coupling (λ_α) is much more influential than the intrasite electron-lattice coupling (λ_β) in the presence of strong on-site repulsion (U_d) at Cu sites.*

H. Parameter dependence of static interaction potential between small polarons

To determine an effective static interaction potential between the small polarons, we calculated the total energies of two-hole-doped systems in which two small polarons are located with various possible relative distances. In the reference parameter set, the two small polarons are repulsive and the potential decays exponentially with the relative distance (Fig. 12). In the present periodic 6×6 system, the longest distance is $3\sqrt{2}$ in units of the Cu-Cu lattice spacing. The total energies in Figs. 12–15 are relative quantities from which the total energy for the longest-distance case has already been subtracted. When the two polarons are located diagonally with distance $3\sqrt{2}$, they occupy Cu sites in the same sublattice of the AF configuration so as to flip or suppress two Cu spins with the same direction. Actually the total energy becomes the lowest when the two polarons occupy Cu sites in different sublattices and they are as far from the other as possible (with distance $\sqrt{13}$). But the energy difference from the longest-distance case is on the order of $10^{-4}t_{pd}$. When the two small polarons are located on the nearest-neighbor Cu sites, the system is unstable (though a self-consistent HF solution is obtained). We plot this case in Fig. 12 for clearer demonstration of the exponential behavior. We do not plot the data in Figs. 13–15 when the HF states are unstable.

As λ_α increases, the horizontally placed small polarons (with distances 1 and 2) repel more strongly, while the repulsion between the (nearly) diagonally placed small polarons (with distances $\sqrt{2}$ and $\sqrt{5}$) shows a maximum around $\lambda_\alpha \simeq 0.3$ (Fig. 13). The two small polarons located on the nearest-neighbor Cu sites become metastable when λ_α exceeds a sufficient value. Finally the small polarons at the next-nearest-neighbor Cu sites achieve lower energy than the longest-distance case, indicating a clumping tendency for $\lambda_\alpha \gtrsim 1.0$, i.e., $\lambda_\alpha \lesssim \lambda_{\alpha c}$. The behavior of the static interaction potential is complicated due to two competing effects: (i) When polarons are on the same sublattice, they can share a local breathing-mode lattice distortion (local CDW); and (ii) when they are on the different sublattices, they flip (or suppress) spins of the opposite directions so that the z component of the total spin remains zero. For the polarons at the nearest- or next-nearest-neighbor Cu sites, the former can reduce repulsion in the d_{xy} channel near the CDW instability (by sharing a charge bag); meanwhile, the latter can reduce repulsion in the $d_{x^2-y^2}$ channel in the SDW background (by sharing a spin bag[28]). As far as the mean-field, static results are concerned, the former seems more effective than the latter for small polarons in close proximity. This reduction of repulsion, i.e., relative attraction due to sharing a bag in the strong repulsive background, might be relevant to a pairing mech-

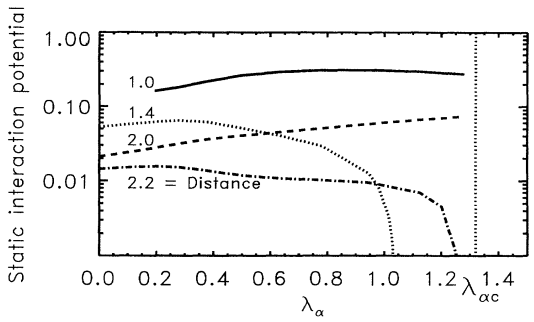

FIG. 13. Total energy for the two-hole-doped systems with several interpolaron distances, relative to the longest-distance case, as a function of λ_α. The other parameters are the same as in Fig. 12.

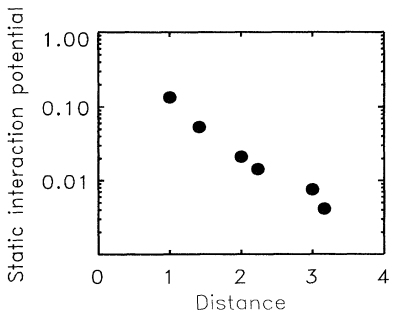

FIG. 12. Total energy for the two-hole-doped systems as a function of the distance between the two small polarons. The energy for the longest-distance case is subtracted. Note the logarithmic scale. Parameters are $t_{pd} = 1$, $t_{pp} = 0.5$, $\Delta = 3$, $U_d = 8$, $U_p = 3$, $U_{pd} = 1$, and $\lambda_\alpha = \lambda_\beta = 0$.

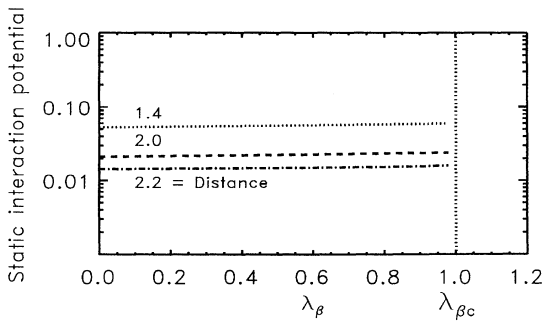

FIG. 14. Total energy for the two-hole-doped systems with several interpolaron distances, relative to the longest-distance case, as a function of λ_β. The other parameters are the same as in Fig. 12.

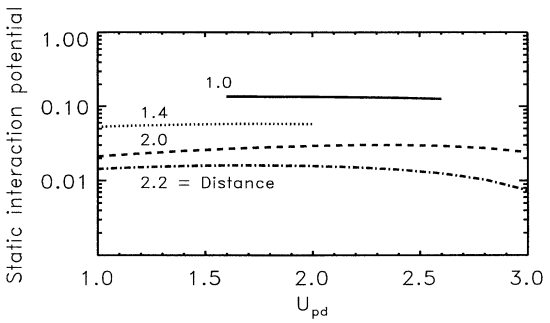

FIG. 15. Total energy for the two-hole-doped systems with several interpolaron distances, relative to the longest-distance case, as a function of U_{pd} with $\Delta = 3.5 - \frac{U_{pd}}{2}$. The other parameters are the same as in Fig. 12.

anism. Here dynamics is of course not taken into account: Bloch-wave-like motion of polarons and possible attraction due to a retardation effect are beyond the scope of the present mean-field theory.

As λ_β increases, the repulsion between the small polarons increases slightly, but they are insensitive to λ_β until it is very close to $\lambda_{\beta c}$ (Fig. 14). This is consistent with the insensitivity of hole-doping states to λ_β discussed above.

As U_{pd} increases with $\Delta + \frac{U_{pd}}{2} = 3.5$, the repulsion between the small polarons slightly increases and shows a maximum around $U_{pd} \simeq 2$ (Fig. 15). For larger U_{pd} values, the small polarons at short distances do not achieve lower energy than the longest-distance case as in the case of increasing λ_α. Rather, they become unstable. This happens at U_{pd} values where hole clumping or phase separation occurs (Sec. III D), thus indicating instability of isolated small polarons toward these clumped states. Indeed, at U_{pd} values where phase separation occurs, the small polarons become unstable accompanied by spin frustration (deviation of spin densities from the collinear configuration) and lowering of energy.

IV. RPA EXCITATION SPECTRA

The different doping states described above have individual spectroscopic signatures in optical and IR absorption, which we now discuss.

For this purpose we consider quantum fluctuations around the mean-field states, by linearizing the equations of motion of particle-hole excitations and phonons. Details are described in Appendix B. Excitation energies $E_n - E_0$ and their eigenfunctions are obtained by solving the RPA equation

$$M \begin{pmatrix} \psi^{(n)*} \\ \varphi^{(n)*} \end{pmatrix} = (E_n - E_0) \begin{pmatrix} \psi^{(n)*} \\ -\varphi^{(n)*} \end{pmatrix} , \qquad (8)$$

where the matrix M is given in Appendix B and depends on the HF energy levels, their wave functions, the bare phonon frequencies, their eigenfunctions, and the parameter values in the interaction part of the model Hamiltonian. Any Green's function which is two body with respect to electrons or one body with respect to phonons (termed "two-body" Green's function) is easily obtained after solution of the RPA equation.

It was shown by Thouless that the linearized equation of motion (the RPA equation) for the particle-hole excitations (in other words, the infinitesimal part of the time-dependent HF equation) is the same as is obtained by the Bethe-Salpeter equation for the particle-hole pairs with the lowest interaction vertex, in which both direct and exchange terms are taken into account.[29] It is easily extended to the present model for electrons and phonons. For later convenience, the diagrammatic derivation is presented in Appendix C.

We obtained all the eigenvalues and their eigenvectors in Eq. (8) by solving Hermitian eigenvalue problems twice, as shown in Appendix D. We note that a comparison of this inhomogeneous HF plus RPA method[22] and exact-diagonalization study[4] for the 2D three-band Hubbard model shows that overall structures in optical and magnetic excitation spectra of the latter method are well reproduced by the former one. Our approach has also been used for a 1D two-band spinless fermion model[24] and again reproduced features of exact optical excitation spectra[23] quite well.

Here various RPA excitation spectra are studied for the undoped and one-hole doped systems. Note that both optical and IR absorption spectra are obtained on the same footing. Single-hole excitation spectra are also calculated within the HF approximation since they are useful for interpreting the RPA excitation spectra. To investigate all linear excitations, we use a small system of 2×2 CuO_2 unit cells and $t_{pp} = 0$ only in this section. (The one-hole-doped systems thus correspond to 25% doping.) If we take the reference parameter set and turn on the intersite electron-lattice coupling (λ_α), the one-hole-doped system varies from a uniform ferromagnetic state for $\lambda_\alpha = 0$, 0.125, to the small-polaron state for $\lambda_\alpha = 0.500$, 1.125 (before destruction of the stoichiometric AF state). To mimic the 6×6 system, we replace $t_{pp} = 0.5$ by $t_{pp} = 0$, for which a similarly rapid crossover from the Zhang-Rice regime to the covalent molecular regime is observed to occur for similar λ_α values in the AF background.

As for the HF results in the previous section, the RPA excitation spectra are insensitive to the intrasite electron-lattice coupling (λ_β) until it is very close to the critical strength $\lambda_{\beta c}$ for destruction of the AF background. So we show here the λ_α dependence of the RPA particle-hole–phonon excitation spectra together with the HF single-hole excitation spectra, for $t_{pp} = 0$, $\lambda_\alpha \neq 0$, and the otherwise reference parameter set.

A. Undoped case

For the undoped systems, the single-hole excitations [Fig. 16(a)] are clearly distinguished into the upper Hubbard band (UHB), the upper part of the bonding oxygen band (UBO), the nonbonding oxygen band (NBO) (recall that $t_{pp} = 0$ here), the lower part of the bonding oxygen band (LBO), and the lower Hubbard band (LHB).[22]

Here we use the hole description for these bands, too. Note that the previous studies[4,22] used the electron description for the bands, so that UHB (LHB) and UBO (LBO) correspond to LHB (UHB) and LBO (UBO) in this paper. The charge-transfer gap refers to the gap between the LHB and the LBO. The HF single-hole excitation spectrum is unchanged for $\lambda_\alpha < \lambda_{\alpha c}$ in the undoped case.

The RPA particle-hole excitation spectra change little with different λ_α values if they are smaller than $\lambda_{\alpha c}$. Only renormalized (RPA) phonon frequencies decrease with increasing λ_α. Note that phonons are mixed with particle-hole excitations to lower their frequencies, but the weight of particle-hole excitations are much smaller than that of phonons in these renormalized phonons.

The spectral weight for AF magnetic excitations at Cu sites,

$$(\pi/N_{\rm cell}) \sum_{n\neq 0} |\langle 0 | \hat{S}^{\perp}_{\rm Cu}(Q) | n\rangle|^2 \, \delta(\omega - (E_n - E_0)) \ ,$$

is shown in Fig. 16(b) in the undoped case, where

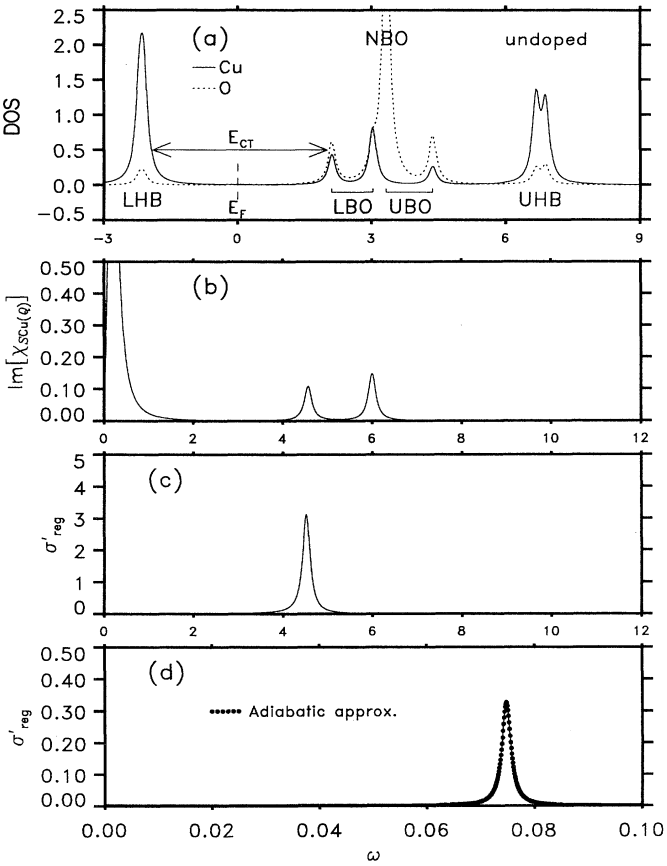

FIG. 16. (a) Spectral weight for single-*hole* excitations, (b) spectral weight for AF magnetic excitations at Cu sites, (c) optical absorption spectra, and (d) IR absorption spectra, for the undoped 2×2 system. Parameters are $t_{pd} = 1$, $t_{pp} = 0$, $\Delta = 3$, $U_d = 8$, $U_p = 3$, $U_{pd} = 1$, $\lambda_\alpha = 0.5$, $\lambda_\beta = 0$, and $K = 32t_{pd}/\text{Å}^2$.

$\hat{\mathbf{S}}_{\rm Cu}(Q) = \sum_{i\in{\rm Cu}}(-1)^i \frac{1}{2}\hat{\boldsymbol{\sigma}}_i$ and $\hat{\boldsymbol{\sigma}}_i = \sum_{\tau,\tau'} c^\dagger_{i\tau}\boldsymbol{\sigma}_{\tau\tau'}c_{i\tau'}$ with $\boldsymbol{\sigma}$ standing for Pauli matrices, the superscript $\perp$ for the transverse components, and $N_{\rm cell}$ for the number of CuO_2 units. Each peak is broadened with a Lorentzian of width 10^{-1}. The peak at $\omega = 0$ is due to the Goldstone modes, which are related to restoration of the spin rotation symmetry broken in the HF solution. The spectral weight at $\omega = 0$ is set to zero for technical convenience[22] using the retarded Green's function. In the thermodynamic limit (and zero temperature), when the AF spin configuration on Cu sites has long-range order, spin-wave excitations are expected with dispersion extending from zero to finite energy. However, for a finite system with a nondegenerate (singlet) ground state, a finite spin gap is generally expected in the exact spectra, which may disappear in the thermodynamic limit. Many particle-hole pairs (corresponding to pairs of unoccupied and occupied HF eigenstates) contribute to the Goldstone modes, reflecting their collective nature. The peaks at $\omega = 4.6$ and $\omega = 6.0$ are due to modes, to which a few particle-hole pairs principally contribute, so that their energies are in the range of (noninteracting) HF particle-hole pair excitation energies. These particle-hole pairs correspond to HF eigenstates in the LHB and in the LBO (LHB $\rightarrow$ LBO transitions).

The real, regular part (i.e., excluding $\omega = 0$) of the conductivity,

$$(\pi/\omega N_{\rm cell}) \sum_{n\neq 0} |\langle 0 | j^{\parallel} | n\rangle|^2 \, \delta(\omega - (E_n - E_0)) \ ,$$

is shown in Figs. 16(c) and 16(d), where $\mathbf{j}$ is given in Eqs. (E7), (E8), and (E9) and the superscript $\parallel$ denotes the components on the CuO_2 plane. For a detailed discussion on the interaction of the system with radiation and resultant conductivity, see Appendix E. Figure 16(c) shows overall structure broadened with a Lorentzian of width 10^{-1}, while Fig. 16(d) shows enlarged phonon-frequency-range structure broadened with a Lorentzian of width 10^{-3}. The main optical absorption peak at $\omega = 4.5$ is due to charge-transfer modes. The particle-hole pairs which contribute to them correspond to LHB $\rightarrow$ NBO transitions. The main IR absorption peak at $\omega = 0.075$ is due to renormalized phonons with symmetry of x or y, which are mixed with particle-hole pairs corresponding to LHB $\rightarrow$ NBO transitions. These IR-active phonon modes and the charge-transfer modes are thus related to each other by the electron-lattice coupling, which lowers the renormalized phonon frequencies. The correlation between the IR-active phonon modes and the charge-transfer modes will become much clearer in the one-hole-doped case discussed below.

B. One-hole-doped case

When one hole is added to the stoichiometric system, it produces a small polaron accompanied by the two localized HF eigenstates inside the charge-transfer gap [Fig. 17(a)]. They correspond to those shown in Fig. 7(b). The higher one (L_h) corresponds to the symmetric O

state formed by the four O orbitals around the central Cu site and has small weight on the Cu site. [Note that the O density of states (DOS) in Fig. 17(a) was averaged over the two O positions.] The lower one (L_l) corresponds to the central Cu state, has small weight on the surrounding O sites, and has opposite spin to the L_h. The bonding counterparts of the L_h and the L_l, L_{bh}, and L_{bl}, are also seen between the UHB and the UBO. (The L_{bh} and the L_{bl} are less distinctive than the L_h and the L_l, as concerns their contribution to the RPA spectra, and so we do not distinguish them from the UHB and the UBO, respectively, for the later analysis of the RPA spectra.) As λ_α increases, the two localized HF eigenstates become nearly degenerate and their associated wave functions have substantial weight both on the central Cu site and on the surrounding O sites [Fig. 18(a)]. L_h and L_l are indistinguishable in their energies and are termed L. They have similar wave functions but different spins. As λ_α increases further, the energies of the localized HF eigenstates are lowered with increasing local covalency. Note that they correspond to the antibonding combination of the central Cu state and the symmetric O state (Sec. III F). In Fig. 19(a), the two

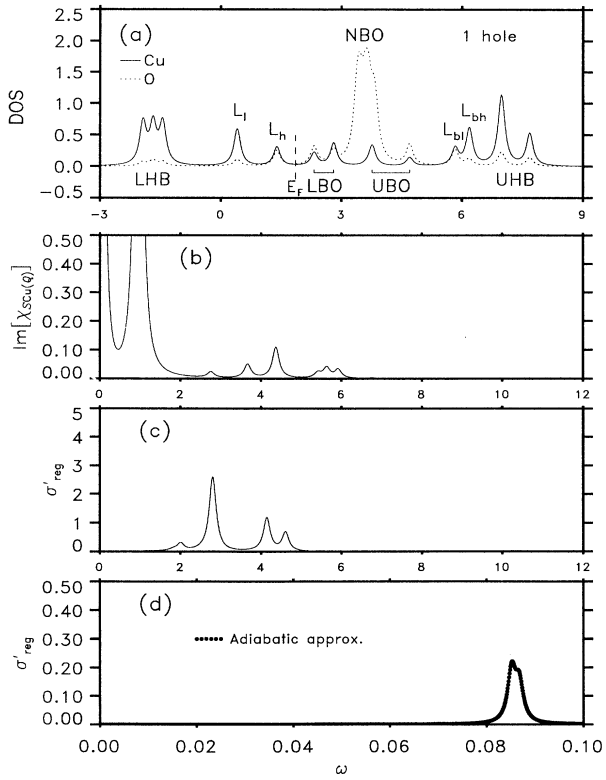

FIG. 17. (a) Spectral weight for single-*hole* excitations, (b) spectral weight for AF magnetic excitations at Cu sites, (c) optical absorption spectra, and (d) IR absorption spectra, for the one-hole-doped 2 × 2 system with a small polaron (Zhang-Rice regime). Parameters are $t_{pd} = 1$, $t_{pp} = 0$, $\Delta = 3$, $U_d = 8$, $U_p = 3$, $U_{pd} = 1$, $\lambda_\alpha = 0.125$, $\lambda_\beta = 0$, and $K = 32t_{pd}/\text{Å}^2$.

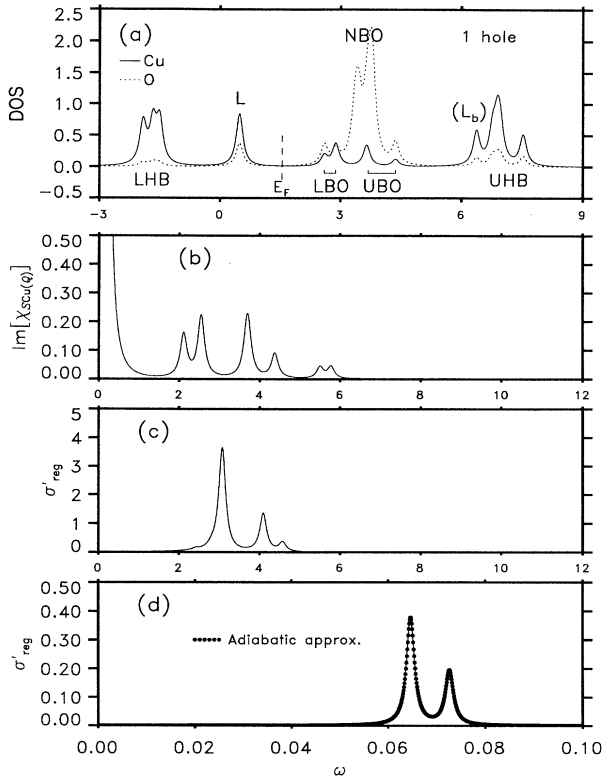

FIG. 18. (a) Spectral weight for single-*hole* excitations, (b) spectral weight for AF magnetic excitations at Cu sites, (c) optical absorption spectra, and (d) IR absorption spectra, for the one-hole-doped 2 × 2 system with a small polaron (crossover regime). Parameters are $t_{pd} = 1$, $t_{pp} = 0$, $\Delta = 3$, $U_d = 8$, $U_p = 3$, $U_{pd} = 1$, $\lambda_\alpha = 0.500$, $\lambda_\beta = 0$, and $K = 32t_{pd}/\text{Å}^2$.

localized HF eigenstates are located just above the LHB. A new peak (L_b) which appears above the UHB corresponds to those other localized HF eigenstates which consist of the bonding combination of the central Cu state and the symmetric O state.

The spectral weight for AF magnetic excitations at Cu sites [Fig. 17(b)] shows new peaks at $\omega = 0.9$, 2.8, and 3.7 which are related to the appearance of the localized HF eigenstates. The particle-hole pairs which mainly contribute to the mode at $\omega = 0.9$ correspond to $L_h \rightarrow$ LBO transitions, those at $\omega = 2.8$ to $L_h \rightarrow$ UBO, and those at $\omega = 3.7$ to $L_l \rightarrow$ UBO. Accordingly, the peaks observed in the undoped case (one at $\omega = 0$ due to the Goldstone mode and the others at $\omega = 4.4$ and $5.4 < \omega < 5.9$ due to modes which are mainly associated with LHB $\rightarrow$ LBO transitions) are bleached. When λ_α is increased and the two localized HF eigenstates are nearly degenerate, the spectral weight [Fig. 18(b)] shows doping-induced peaks at $\omega = 2.1$, 2.5, and 3.7. Their corresponding modes are mainly associated with $L \rightarrow$ LBO, $L \rightarrow$ UBO, and $L \rightarrow$ UBO transitions, respectively. When λ_α is further increased and the two localized HF eigenstates are located just above the LHB, the spectral weight [Fig. 19(b)] shows a doping-induced peak at

$\omega = 6.9$, which has higher energy than the stoichiometric LHB $\rightarrow$ LBO peaks. There is no doping-induced structure on their low-energy side in this magnetic channel, as in Figs. 17(b) and 18(b). In fact, the corresponding modes are mainly associated with $L \rightarrow L_b$ transitions.

The real, regular part of the conductivity also shows new peaks induced by doping. In the optical absorption spectrum [Fig. 17(c)], new peaks are induced at $\omega = 2.0$ and $\omega = 2.8$ which are again related to the appearance of the localized HF eigenstates. The particle-hole pairs which mainly contribute to the mode at $\omega = 2.0$ correspond to $L_h \rightarrow$ NBO transitions and those at $\omega = 2.8$ to $L_l \rightarrow$ NBO. Accordingly, the peak observed in the undoped case, which is associated with LHB $\rightarrow$ NBO transitions, is split and bleached. A similar spectrum is observed when the two localized HF eigenstates are nearly degenerate [Fig. 18(c)]. However, when they are located just above the LHB [Fig. 19(c)], a doping-induced peak appears at $\omega = 4.8$, which is higher than the stoichiometric LHB $\rightarrow$ NBO peak. But a doping-induced peak does not appear on its low-energy side as in Figs. 17(c) and 18(c). The corresponding modes are mainly associated with $L \rightarrow$ NBO transitions.

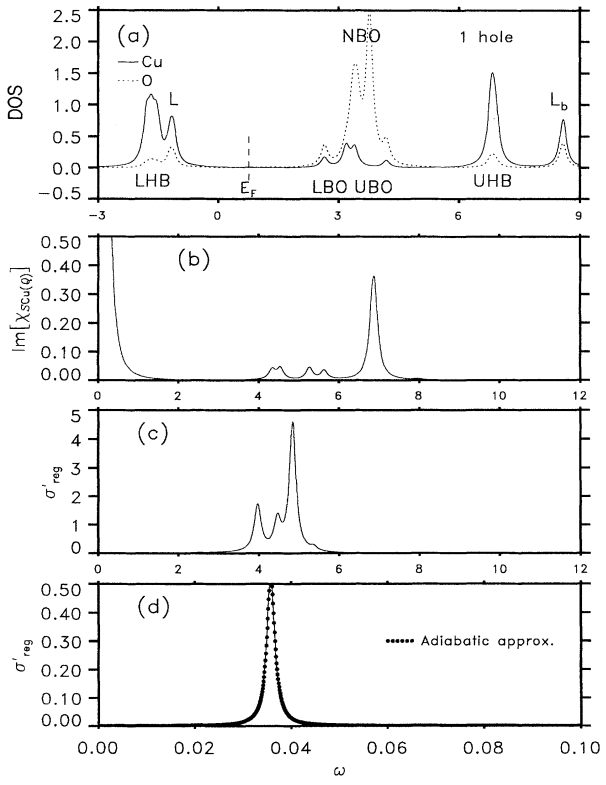

FIG. 19. (a) Spectral weight for single-*hole* excitations, (b) spectral weight for AF magnetic excitations at Cu sites, (c) optical absorption spectra, and (d) IR absorption spectra, for the one-hole-doped 2 × 2 system with a small polaron (covalent molecular regime). Parameters are $t_{pd} = 1$, $t_{pp} = 0$, $\Delta = 3$, $U_d = 8$, $U_p = 3$, $U_{pd} = 1$, $\lambda_\alpha = 1.125$, $\lambda_\beta = 0$, and $K = 32t_{pd}/\text{Å}^2$.

In the IR absorption spectrum [Fig. 17(d)], there are two peaks at $\omega = 0.085$ and $\omega = 0.087$, while the stoichiometric peak is only at $\omega = 0.088$ (not shown). Two phonons contribute to the mode at $\omega = 0.085$. One corresponds to the antisymmetric oscillation of the right and left O atoms neighboring the central Cu site of the small polaron. The other corresponds to the antisymmetric oscillation of the up and down O atoms neighboring the central Cu site. Thus the two O atoms on the horizontal Cu-O-Cu bonds inside the polaron move in the same direction in the former case, as do those on the vertical Cu-O-Cu bonds in the latter case. These phonons are mixed with particle-hole pairs corresponding to $L_h \rightarrow$ NBO and $L_l \rightarrow$ NBO transitions more strongly than those corresponding to LHB $\rightarrow$ NBO transitions. In other words, the local phonons are more strongly mixed with local particle-hole excitations than extended ones. Two phonons contribute to the mode at $\omega = 0.087$: namely, with the O atoms on the horizontal Cu-O-Cu bonds *outside* the polaron moving in the same direction and those on the outer vertical Cu-O-Cu bonds moving in the same direction. They are mixed with particle-hole pairs corresponding to LHB $\rightarrow$ NBO transitions more strongly than those corresponding to $L_h \rightarrow$ NBO and $L_l \rightarrow$ NBO transitions. When λ_α is increased and the two localized HF eigenstates are nearly degenerate [Fig. 18(d)], the frequencies of the local IR-active phonon modes ($\omega = 0.065$) are well split, downward from that of the extended ones ($\omega = 0.073$). Here local phonons are mixed more strongly with local particle-hole excitations and extended phonons with extended particle-hole excitations. This particular mixing is more distinct than the case of Fig. 17(d) where the phonon frequency difference is small. When λ_α is further increased and the two localized HF eigenstates are located just above the LHB [Fig. 19(d)], the frequency difference between the local-IR active phonon modes ($\omega = 0.036$) and the extended ones ($\omega = 0.036$) becomes very small. Accordingly, the particular mixing of phonons and particle-hole excitations becomes much less distinct. Note that the difference between the IR-active phonon modes and the IR-*inactive* ones is large here. That is, both local and extended IR-active phonon modes are nearly equally softened by the electron-lattice coupling.

Finally, the following observation should be added. Earlier, Rice and Wang have used a simple electron-phonon model, which includes a single Cu orbital, four surrounding O orbitals, and the same intersite electron-lattice coupling as our λ_α coupling, to study a combined excitonic and "charged phonon" mechanism.[30] They calculated absorption spectra due to the electronic and vibronic excitations on the same footing, with the use of an RPA formula (as obtained along the lines of Appendixes F, G, and I without the adiabatic assumption). The parameters were chosen by fitting to experimental data — their model is for the absorption spectra. The mechanism of how the phonon modes achieve their IR activity is the same as ours as far as the phonon-assisted, electronic contribution is concerned. (See Appendixes E and I for another possibility of phonon contribution, which would be negligible for organic conduc-

tors but should be taken into account for ionic materials: Our calculation includes both contributions.) In our study, magnetic excitation spectra are also obtained on the same footing, and therefore parameters can be deduced from additional experiments.

C. Validity of adiabatic approximation

We also calculated the IR absorption spectra, using the adiabatic approximation. Details are discussed in the next section. Our purpose here is to demonstrate how it works in the phonon-frequency range within the RPA.

The resultant IR absorption spectra are plotted with dotted lines in Figs. 16(d), 17(d), 18(d), and 19(d). They are on the solid lines obtained without the use of the adiabatic approximation. This clearly shows that the adiabatic approximation works excellently for the present IR absorption spectra.

V. ADIABATIC EXCITATION SPECTRA

For response functions in the phonon-frequency range, the adiabatic approximation can be used to distinguish phonon excitations from particle-hole excitations in charge-transfer-energy or higher-energy ranges.[31,32] As long as the charge-transfer energy and any other particle-hole excitation energies are much higher than the phonon frequencies (adiabatic condition), this approximation is good. This has been numerically checked in the previous section by comparing the RPA excitation spectra and the adiabatic excitation spectra in the phonon-frequency range.

The low-energy excitations can then be regarded as phonons dressed by particle-hole polarization through electron-phonon interaction. The dressed holes interact with each other through electron-electron interaction. When the spin rotation symmetry is broken, there is another type of low-energy excitations, i.e., spin waves, whose energy reaches to zero (Goldstone mode). In the RPA scheme, phonons can interact with charge excitations while spin waves are transverse spin excitations.[21] Thus the presence of spin waves does not jeopardize the adiabatic approximation.

The value of the HF-orbital representation (Appendixes B and C) is lost since electronic excitations are not of interest here. Instead, the real-space representation becomes useful since it needs a much smaller basis. The RPA equation in the latter representation is derived in Appendix F.

When the above adiabatic condition holds, the electron-electron, the phonon-phonon, and the other components of the "two-body" Green's function can be treated differently. It is convenient to define an electronically renormalized electron Green's function $\Pi_E(\omega)$ and write each component of the "two-body" Green's function in terms of it, as described in Appendix G.

On the time scale characteristic of lattice vibrations, the holes instantaneously move toward the lowest-energy state at each (time-dependent) lattice configuration. On the time scale of electronic motion, the lattice is frozen. Thus we can neglect the frequency dependence of the electronically renormalized electron Green's function $\Pi_E(\omega)$ by setting $\omega = 0$. Eigenfrequencies ω_ν and their eigenfunctions $\gamma_\nu(k)$ of the renormalized phonons are obtained by diagonalizing the renormalized spring-constant matrix (divided by the ionic mass),

$$\sum_l \frac{1}{\sqrt{M_k}} K_{kl}^{\rm ren} \frac{1}{\sqrt{M_l}} \gamma_\nu(l) = \omega_\nu^2 \gamma_\nu(k) \quad , \tag{9}$$

where

$$K^{\rm ren} = K + K_{PE} \Pi_E(\omega = 0) K_{EP} \quad , \tag{10}$$

with the bare spring-constant matrix K appearing in the Hamiltonian, Eq. (1), and the phonon-electron and electron-phonon components of the kernel, K_{PE} and K_{EP}, defined in Eq. (F8) and depending only on the parameter values in the interaction part of the model Hamiltonian. This is derived in Appendix H.

For IR absorption spectra, we need to consider how the model system interacts with radiation. Details are described in Appendix E. The dipole moment is assumed to be defined by

$$\mathbf{P} = \sum_i (\mathbf{r}_i + \mathbf{u}_i) \left(Z_i + \sum_\sigma c_{i\sigma}^\dagger c_{i\sigma} \right) \quad , \tag{11}$$

with $\mathbf{r}_i$ standing for the equilibrium positions of atoms, $\mathbf{u}_i$ for the lattice displacements, Z_i for the charge not explicitly included in the model, and $(Z_i + \sum_\sigma c_{i\sigma}^\dagger c_{i\sigma})$ for the ionic charge. We take $Z_i = +1$ for the Cu sites and $Z_i = -2$ for the O sites. The paramagnetic current is given by

$$\mathbf{j} = i[H, \mathbf{P}] = i \sum_{i,j,\sigma} (\boldsymbol{\epsilon}_{ij} + \mathbf{u}_j - \mathbf{u}_i) t_{ij}(\{\mathbf{u}_k\}) c_{i\sigma}^\dagger c_{j\sigma} + \sum_i \frac{\mathbf{p}_i}{M_i} \left(Z_i + \sum_\sigma c_{i\sigma}^\dagger c_{i\sigma} \right) \quad , \tag{12}$$

where $\boldsymbol{\epsilon}_{ij} = \mathbf{r}_j - \mathbf{r}_i$, and $\mathbf{p}_i$ denotes the conjugate momentum to $\mathbf{u}_i$. Note that $\mathbf{u}_i$ and $\mathbf{p}_i$ are the same as the corresponding quantities without the vector notation in Eq. (1) — the vector notation is used here to distinguish the polarization dependence of the absorption or scattering of photons. Conductivity is calculated through the (paramagnetic) current-current correlation function, as explained in Appendix I. Calculations were made for systems of 6×6 CuO_2 unit cells again. One-hole-doped systems correspond to 2.8% doping. Therefore relative strengths of doping-induced absorptions are much weaker than those in Sec. IV.

A. Hole-doped case

For the states with a small polaron, the IR absorption spectrum changes with the intersite electron-lattice coupling (λ_α), as shown in Fig. 20. The other parameters are the same as the reference parameter set. Here we used $K = 32 t_{pd}/\text{Å}^2 \simeq 42$ eV/Å^2. This gives, in the absence of electron-lattice coupling, dispersionless phonons with

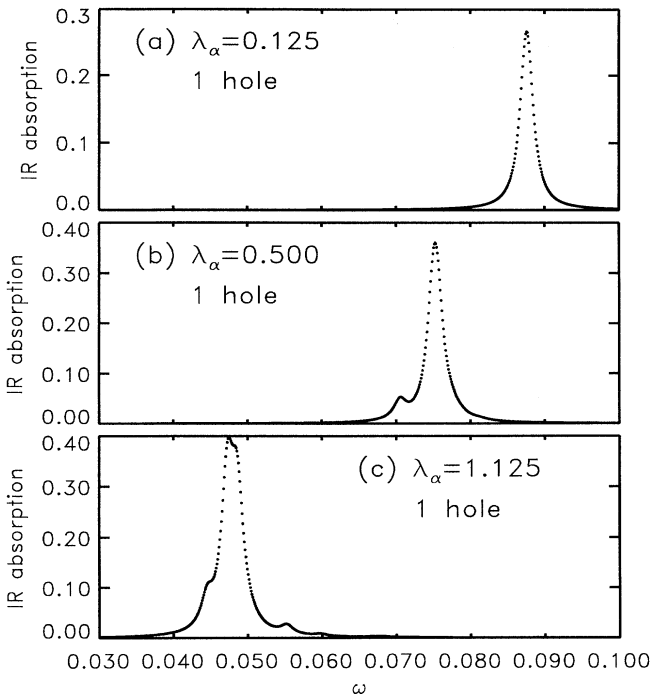

FIG. 20. IR absorption spectra for the one-hole-doped systems with a small polaron. (a) $\lambda_\alpha = 0.125$, (b) $\lambda_\alpha = 0.500$, and (c) $\lambda_\alpha = 1.125$. The other parameters are as in Fig. 7.

frequency $0.0914 \simeq 840\ \mathrm{cm}^{-1}$ and a single peak in the IR spectrum due to two extended modes, which oscillate O atoms uniformly in the respective x and y directions. (In terms of Appendix I, this is purely due to the phonon contribution because of the absence of electron-lattice coupling. For details, see Appendix E.) Note that, as the coupling increases, phonons are softened and their frequencies decrease, including the IR-active phonon modes. The δ peaks have been broadened with Lorentzians of width 10^{-3}.

For $\lambda_\alpha = 0.125$, the peak ($\omega = 0.088$) is mainly due to extended modes which oscillate O atoms almost uniformly in the x or y direction but weakly around the small polaron [Fig. 20(a)]. There are local IR-active phonon modes ($\omega = 0.086$) corresponding to the antisymmetric oscillations of pairs of O atoms in the small polaron, as in Fig. 17(d). That is, the two O atoms on the horizontal Cu-O-Cu bonds inside the polaron move in the same direction in one mode, as do those on the vertical Cu-O-Cu bonds in the other mode. There is another type of IR-active phonon modes (also at $\omega = 0.088$) which are extended in the direction of oscillation and localized in the other direction so that we term them semilocal modes. But both the local and semilocal modes are indistinguishable in the IR absorption spectra, hidden by the broadening for the extended modes.

For $\lambda_\alpha = 0.500$, a doping-induced peak due to the local IR-active phonon modes ($\omega = 0.071$) is well split from the main peak due to the extended ones ($\omega = 0.076$) and clearly visible [Fig. 20(b)]. The semilocal modes ($\omega = 0.075$) are still indistinguishable in the spectrum from the extended modes. This spectrum is qualitatively consistent with the experimentally observed[16] bleaching of phonon modes and intensity shift to lower frequencies following photoexcitation. Also observed in the same experiments[16] is a bleaching of the interband electronic absorption and the corresponding activation of an electronic absorption in the gap, which we can qualitatively associate with the appearance of gap states [Fig. 7(b)].

For $\lambda_\alpha = 1.125$, both peaks due to the local modes ($\omega = 0.045$) and the semilocal modes ($\omega = 0.047$) are split from the peak coming from the extended modes ($\omega = 0.049$) [Fig. 20(c)]. Here the oscillator strength of the semilocal modes is largest and those of the local and extended modes are seen as shoulders on the low- and high-frequency sides, respectively. Furthermore, extended modes which do *not* uniformly oscillate O atoms develop IR activity at $\omega = 0.055$ and $\omega = 0.060$. When λ_α is close to, but smaller than $\lambda_{\alpha c}$, even the stoichiometric phonons have a nonsmooth dispersion relation, which is reminiscent of a transition by breaking of analyticity.[33]

For the state with an intermediate-size polaron ($U_d = 10$, $\Delta = 4$, $\lambda_\alpha = 0.125$, and the otherwise reference parameter set), the IR absorption spectrum (Fig. 21) is quite different from those for the small-polaron states. The weaker peak ($\omega = 0.088$) is due to extended modes which oscillate O atoms almost uniformly in the x or y direction but weakly around the intermediate-size polaron. The stronger peak ($\omega = 0.077$) is due to local modes which oscillate mainly the four O atoms bridging the four Cu sites in the polaron (Fig. 3). The amplitudes of the associated eigenfunctions decay with distance from the polaron. In a previous report[9] a spectrum for the same state is shown, in which the peak due to the extended modes is much weaker. This is due to the fact that the second term of Eq. (12) was omitted there. There is in fact some uncertainty in defining the current operator because the model Hamiltonian does not completely describe how the ionic charge follows the motion of the corresponding atom. For details, see Appendix E. In terms of Appendix I, the oscillator strengths of the extended modes are mainly due to the phonon contribution, while those of the local modes are mainly due to the phonon-assisted electronic contribution. Indeed, the strong IR activity of the local modes is caused by their

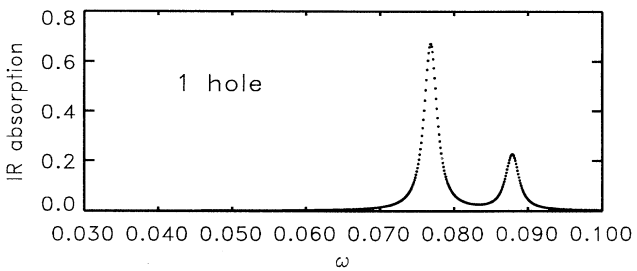

FIG. 21. IR absorption spectra for the one-hole-doped system with an intermediate-size ferromagnetic polaron. $\lambda_\alpha = 0.125$. The other parameters are as in Fig. 9.

mixing with soft particle-hole excitations which are related to the highest occupied HF eigenstate. Note that this gap state is located near the O band and has substantial weight at Cu sites as well as O sites inside the intermediate-size polaron: A charge-transfer process does not require energy comparable with the stoichiometric charge-transfer gap.

B. Electron-doped case

We also studied "electron"-doping states. For the reference parameter set (as in Fig. 1), the electron-doping state contains a small polaron (Fig. 22). A hole is taken away mainly from a single Cu site and partly from the four Cu sites neighboring this central Cu site. The spin density at the central Cu site is small and flipped (to point up). Two HF eigenstates appear deep within the charge-transfer gap per removed hole. Note that both gap states are unoccupied by holes. The lower gap state, which is the lowest unoccupied HF eigenstate, corresponds to the central Cu state with spin up and has small weight on the four neighboring Cu sites. The higher gap state, lying near the center of the gap, corresponds to the central Cu state with spin down and has substantial weight on the four surrounding O sites. Thus the two gap states roughly correspond to those in the hole-doping case. (Note that there is no inherent electron-hole symmetry in our multiband model.) Because the hole density is small at the central Cu site, the central Cu states for both spins have low energy, of which the higher-energy state can mix more with the surrounding O states.

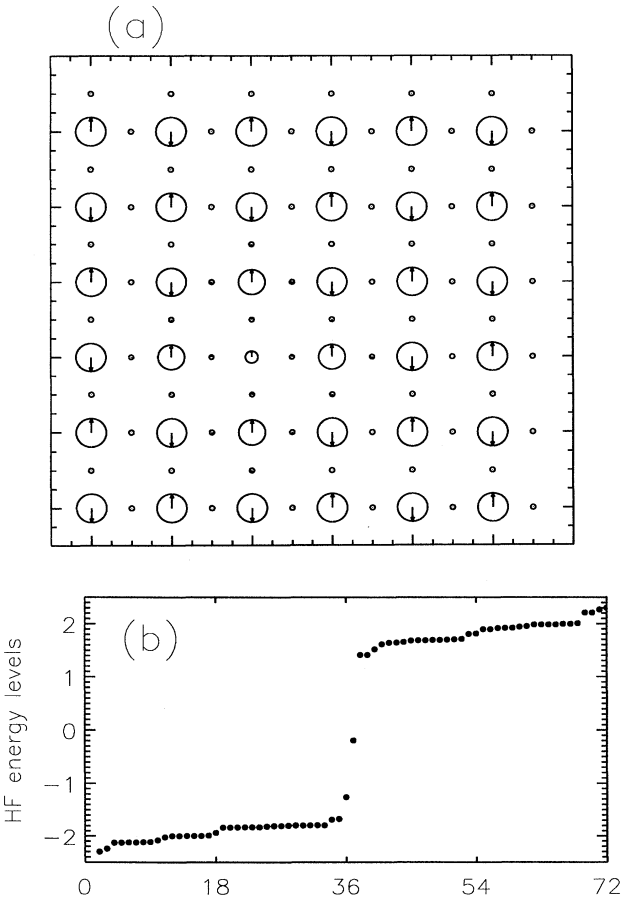

FIG. 22. (a) Spin and charge densities and (b) HF energy levels around the gap for the one-"electron"-doped system with a small polaron. Parameters are $t_{pd} = 1$, $t_{pp} = 0.5$, $\Delta = 3$, $U_d = 8$, $U_p = 3$, $U_{pd} = 1$, and $\lambda_\alpha = \lambda_\beta = 0$. The symbols are as in Fig. 1.

We now consider how the intersite electron-lattice coupling (λ_α) modifies this electron-doping state. For $\lambda_\alpha = 1.125$ and the otherwise reference parameter set (as in Fig. 6), the electron-doping state contains again a small polaron (Fig. 23). The four O atoms are displaced from the central Cu state, enhancing the hopping integral between the four O sites and the surrounding four Cu sites, but reducing that between the four O sites and the central Cu site, and thus transferring hole density from the central Cu site to the four neighboring Cu sites. A hole is taken away almost exclusively from the central Cu site and the hole density is almost zero at this site. We can regard the effect of the intersite electron-lattice coupling (λ_α) as reducing the magnetic moment on the central Cu site through local lattice distortion in both hole- and electron-doping cases. Three HF eigenstates appear inside the charge-transfer gap per removed hole, all of which are unoccupied. Two of them, lying near the center of the gap, correspond mainly to the up- and down-spin central Cu states, due to weakened hopping integrals between the central Cu site and the four surrounding O sites. The up-spin central Cu state has more weight at the central Cu site than the down-spin one because it is incompatible with the lower Hubbard band. The down-spin central Cu state has small weight on the four surrounding O sites. A difference from the hole-doping state is that the two nearly degenerate central Cu states lie near the center of the gap, not near the lower Hubbard band. The other gap state lies near the O band and corresponds to a down-spin symmetric O state formed by the four O states and has small weight on the central Cu site.

For the above electron-doping states with a small polaron, the IR absorption spectrum changes with the intersite electron-lattice coupling (λ_α), as shown in Fig. 24.

For $\lambda_\alpha = 0.125$, the IR peak ($\omega = 0.088$) is mainly due to extended modes which oscillate O atoms almost uniformly in the x or y direction but weakly around the small polaron [Fig. 24(a)]. There are local IR-active phonon modes ($\omega = 0.090$) corresponding to the antisymmetric oscillations of pairs of O atoms in the small polaron. There are also semilocal IR-active phonon modes (also at $\omega = 0.088$) which are extended in the direction of oscillation and localized in the other direction. But both the local and semilocal modes are indistinguishable in the IR absorption spectra, hidden by the broadening for the extended modes.

For $\lambda_\alpha = 0.500$, a doping-induced structure due to the local IR-active phonon modes ($\omega = 0.084$) are well split from the main peak due to the extended ones ($\omega = 0.076$) and are seen as a hump [Fig. 24(b)]. The semilocal modes

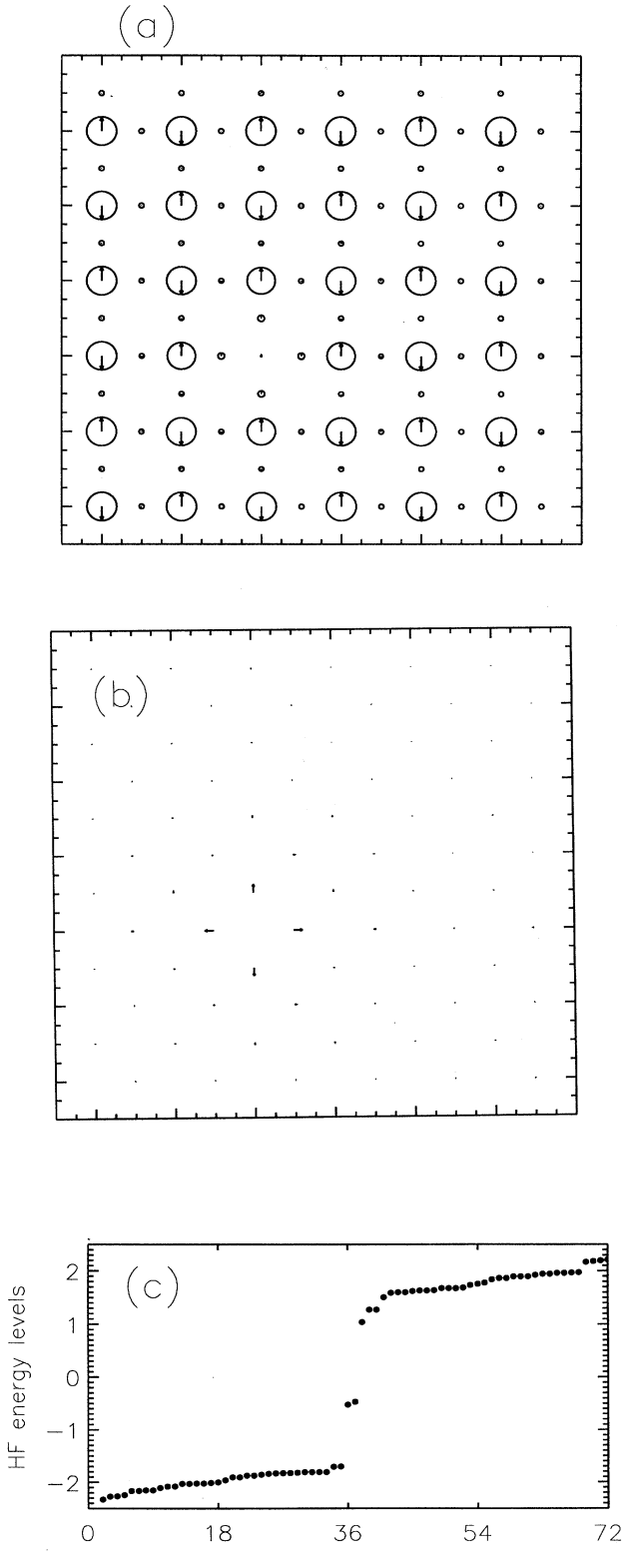

FIG. 23. (a) Spin and charge densities, (b) O-atom displacements, and (c) HF energy levels around the gap for the one-"electron"-doped system with a small polaron. Parameters are $t_{pd} = 1$, $t_{pp} = 0.5$, $\Delta = 3$, $U_d = 8$, $U_p = 3$, $U_{pd} = 1$, $\lambda_\alpha = 1.125$, and $\lambda_\beta = 0$. The symbols are as in Fig. 1.

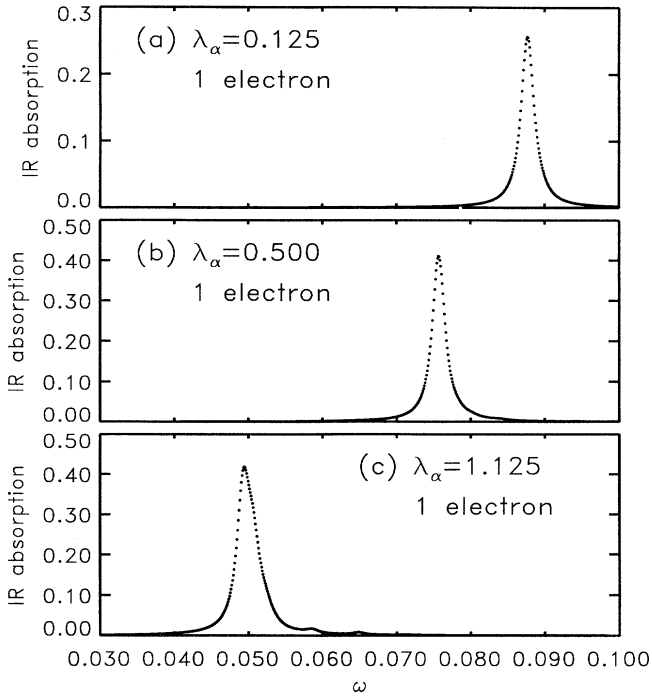

FIG. 24. IR absorption spectra for the one-"electron"-doped systems with a small polaron. (a) $\lambda_\alpha = 0.125$, (b) $\lambda_\alpha = 0.500$, and (c) $\lambda_\alpha = 1.125$. The other parameters are as in Fig. 7.

(also close to $\omega = 0.076$) are still indistinguishable in the spectrum from the extended modes. The oscillator strengths of the local and semilocal modes are much weaker than the corresponding hole-doping case.

For $\lambda_\alpha = 1.125$, a doping-induced structure due to the local IR-active phonon modes ($\omega = 0.071$) are well split from the main peak due to the extended ones ($\omega = 0.049$) and are seen as a very small hump [Fig. 24(c)]. The semilocal modes ($\omega = 0.051$) are seen as a shoulder on the high-frequency side of the main peak. The oscillator strengths of the local and semilocal modes are much weaker than the hole-doping case here, too. Again, extended modes which do *not* uniformly oscillate O atoms develop IR activity at $\omega = 0.059$ and $\omega = 0.065$.

The IR spectra for the electron-doping states are different from those for the hole-doping states in the following ways: (i) The local and semilocal modes have higher frequencies than the extended modes, and (ii) their oscillator strengths are very small. For the electron-doping case, both the phonon contribution and the phonon-assisted, electronic contribution to their oscillator strengths are smaller than those for the hole-doping case. Roughly speaking, both the central Cu site and the four surrounding O sites have little hole density in the electron-doping case, so that the local O-atom vibration has less chance to couple with local particle-hole excitations than the hole-doping case. Consequently, local phonons are less softened through local particle-hole polarization and contribute less to absorption spectra.

Another reason for the difference is that, for the electron-doping case, the phonon contribution and the phonon-assisted, electronic contribution interfere destructively. However, for the hole-doping case, they interfere constructively.

Finally we note, in the electron-doping case, that (i) an intermediate-size polaron does not exist even for large U_d and Δ; this is because the highest occupied HF eigenstate for the stoichiometric case has momentum $(\pi, 0)$, not (0, 0) as for the lowest unoccupied HF eigenstate relevant for the hole-doping state with large U_d and Δ; and (ii) the intrasite electron-lattice coupling (λ_β) modifies the small-polaron state by displacing the four O atoms from the central Cu site and transferring hole density from the central Cu site to the four neighboring Cu sites, as the intersite electron-lattice coupling (λ_α) does. (The local lattice distortion is much larger than the hole-doping case because the difference of hole densities between the central Cu site and the four neighboring Cu sites is large.)

VI. CONCLUSIONS

We have used a convenient inhomogeneous HF plus RPA approach to study hole-doping states and associated electronic and phonon response functions in the 2D three-band extended Peierls-Hubbard model. There are tendencies toward various broken-symmetry ground states — the AF, spin-Peierls, BOW, and CDW phases — with relative strengths depending upon the parameter values of this model. At stoichiometry, one of them — the AF phase for the copper oxides — dominates. We find that deviations from stoichiometry, i.e., doping, enhance these underlying competitions *locally*. Thus hole-doping states may be localized (at a mean-field level) or somewhat extended, and may have a substantially different broken-symmetry character than that of the background in which they reside. As described above, we have found sensitivity to U_d and U_{pd} in this regard, including phase separation and/or clumping.

Strikingly, intersite electron-lattice coupling (λ_α) can quench a Cu magnetic moment and create local lattice distortion in a completely AF background. This occurs in a substantial precursor regime relative to the critical coupling $\lambda_{\alpha c}$ for destruction of the stoichiometric AF state. Thus Hubbard interactions may be strong and λ_α relatively weak — the effects of the electron-lattice coupling are entirely concentrated around the added holes and are not to be measured relative to the global magnetic coupling. However, it induces local phonon modes as well as local particle-hole excitations related to the gap states, so that it should be observed in IR and optical absorption spectra as bleaching of the stoichiometric peaks and an inducing of new peaks. The possible implications for attractive hole interactions or superconductivity remain to be explored. However, our results are clearly directly relevant to the photodoping[16] of holes into the CuO_2 planes of the copper oxides such as $La_{2-x}Sr_xCuO_4$, $YBa_2Cu_3O_{7-\delta}$, $Bi_2Sr_2Ca_{n-1}Cu_nO_y$, $Tl_2Ba_2Ca_{n-1}Cu_nO_y$, and so on. In these materials there is clear evidence for an AF correlation at stoichiometry, but doping induces IR evidence for local lattice distortions, and also for phase separation. Our results demonstrate how such hole-doping effects can indeed be induced in a strong AF background. For the electron-doped Nd_2CuO_{4-y} system also, there is evidence for a bound charge coupled to the nearby spin and lattice excitations.[15]

Furthermore, we have given specific optical and IR absorption signatures for such polaron doping states. A detailed correlation of these predictions with experimental data will not only demonstrate the presence of electron-lattice coupling in the copper oxides but also determine its strength. Specifically, as shown in Figs. 20 and 21, the different doping states show distinctive spectroscopic signatures, which could be used to identify the chemical doping or photodoping states in the copper oxides. Our results have shown that simple lattice dynamics fitting to experimental data is insufficient — the doping states must be determined self-consistently, including electron-electron and electron-lattice couplings, to understand the *correlation* of electronic and phonon signatures. In the real materials, there are of course several phonon branches, including ones with acoustic character, and a variety of electron-lattice couplings. More experimental data, particularly regarding relevant phonon degrees of freedom, are therefore required to exploit fully our method. For example, electron-lattice coupling in the direction perpendicular to the CuO_2 planes has been shown to be very active in the copper oxides.[34]

ACKNOWLEDGMENTS

We would like to thank I. Batistić, N. E. Bickers, J. T. Gammel, R. L. Martin, J. Mustre de Leon, P. Prelovsek, J. Ranninger, H. Röder, D. J. Scalapino, G. A. Thomas, S. A. Trugman, G. Yu, L. Yu, and J. Zaanen for useful discussions. Work at Los Alamos was supported by the U.S. DOE.

APPENDIX A: SELF-CONSISTENCY CONDITIONS FOR THE MEAN-FIELD STATE

Following Eq. (4), the Hamiltonian, Eq. (1), is rewritten as

$$\begin{aligned} H = & \sum_{i\neq j,\sigma} t_{ij}(\{\langle u_k\rangle\})c^\dagger_{i\sigma}c_{j\sigma} + \sum_{i,\sigma} e_i(\{\langle u_k\rangle\})c^\dagger_{i\sigma}c_{i\sigma} \\ & + \sum_{i,j,k,\sigma} \bar{g}^k_{ij}\hat{u}_k c^\dagger_{i\sigma}c_{j\sigma} \\ & + \sum_i U_i c^\dagger_{i\uparrow}c^\dagger_{i\downarrow}c_{i\downarrow}c_{i\uparrow} + \sum_{\langle i\neq j\rangle,\sigma,\sigma'} U_{ij}c^\dagger_{i\sigma}c^\dagger_{j\sigma'}c_{j\sigma'}c_{i\sigma} \\ & + \sum_l \frac{1}{2M_l}p_l^2 + \sum_{k,l}\frac{1}{2}K_{kl}u_k u_l \ . \end{aligned} \tag{A1}$$

For the electronic part, we use the HF approximation which is unrestricted in both spin *and* direct space. To this end, we introduce a canonical transformation

$$c_{i\sigma} = \sum_\lambda c_\lambda \phi_\lambda(i\sigma) \ , \tag{A2}$$

and assume the HF state is specified by the occupancy of the HF orbitals, λ. Here the index λ is for both spin and direct space to allow those HF configurations whose spin densities are not collinear. The normal ordering is defined with respect to the occupancy,

$$c_\lambda^\dagger c_\mu = \delta_{\lambda\mu}\theta(F-\lambda) + N(c_\lambda^\dagger c_\mu) \ , \tag{A3}$$

where $\theta(F-\lambda)$ takes unity if the orbital λ is occupied and zero otherwise. Using the normal ordering of two-body operators,

$$\begin{aligned} c_\lambda^\dagger c_\mu^\dagger c_\nu c_\tau = {} & (\delta_{\lambda\tau}\delta_{\mu\nu} - \delta_{\lambda\nu}\delta_{\mu\tau})\theta(F-\lambda)\theta(F-\mu) \\ & + \delta_{\lambda\tau}\theta(F-\lambda)N(c_\mu^\dagger c_\nu) + \delta_{\mu\nu}\theta(F-\mu)N(c_\lambda^\dagger c_\tau) \\ & - \delta_{\lambda\nu}\theta(F-\lambda)N(c_\mu^\dagger c_\tau) - \delta_{\mu\tau}\theta(F-\mu)N(c_\lambda^\dagger c_\nu) \\ & + N(c_\lambda^\dagger c_\mu^\dagger c_\nu c_\tau) \ , \end{aligned} \tag{A4}$$

we rewrite the Hamiltonian [Eq. (1)] into

$$H = H_c + H_z + H_e + H_p + H_{\rm int} \ , \tag{A5}$$

where the constant term H_c, the term linear in $\hat{u}_k$, H_z, the one-body electronic part H_e, the phonon part H_p, and the interaction part $H_{\rm int}$ are given by

$$\begin{aligned} H_c = {} & \sum_{\lambda\in{\rm occ}} \langle \lambda \mid T(\{\langle u_k\rangle\}) \mid \lambda\rangle + \sum_{k,l}\frac{1}{2}K_{kl}\langle u_k\rangle\langle u_l\rangle \\ & + \frac{1}{2}\sum_{\lambda\in{\rm occ}}\sum_{\mu\in{\rm occ}} (\langle\lambda\mu \mid V \mid \lambda\mu\rangle - \langle\lambda\mu \mid V \mid \mu\lambda\rangle) \ , \end{aligned} \tag{A6}$$

$$H_z = \sum_k \hat{u}_k \left(\sum_{\lambda\in{\rm occ}} \bar{g}_{\lambda\lambda}^k + \sum_l K_{kl}\langle u_l\rangle \right) \ , \tag{A7}$$

$$\begin{aligned} H_e = \sum_{\lambda,\mu} N(c_\lambda^\dagger c_\mu) \Big[& \langle \lambda \mid T(\{\langle u_k\rangle\}) \mid \mu\rangle \\ & + \sum_{\nu\in{\rm occ}} (\langle\lambda\nu \mid V \mid \mu\nu\rangle \\ & - \langle\lambda\nu \mid V \mid \nu\mu\rangle) \Big] \ , \end{aligned} \tag{A8}$$

$$H_p = \sum_l \frac{1}{2M_l}p_l^2 + \sum_{k,l}\frac{1}{2}K_{kl}\hat{u}_k\hat{u}_l \ , \tag{A9}$$

$$\begin{aligned} H_{\rm int} = {} & \sum_{\lambda,\mu,k} \bar{g}_{\lambda\mu}^k \hat{u}_k N(c_\lambda^\dagger c_\mu) \\ & + \frac{1}{2}\sum_{\lambda\mu\nu\tau} \langle\lambda\mu \mid V \mid \nu\tau\rangle N(c_\lambda^\dagger c_\mu^\dagger c_\tau c_\nu) \ . \end{aligned} \tag{A10}$$

The matrix elements of the one- and two-body terms of Eq. (A1) are given by

$$\langle \lambda \mid T(\{\langle u_k\rangle\}) \mid \mu\rangle = \sum_{i\neq j,\sigma} t_{ij}(\{\langle u_k\rangle\})\phi_\lambda^*(i\sigma)\phi_\mu(j\sigma) + \sum_{i,\sigma} e_i(\{\langle u_k\rangle\})\phi_\lambda^*(i\sigma)\phi_\mu(i\sigma) \ , \tag{A11}$$

$$\begin{aligned} \langle\lambda\mu \mid V \mid \nu\tau\rangle = {} & \frac{1}{2}\sum_i U_i[\phi_\lambda^*(i\uparrow)\phi_\mu^*(i\downarrow) - \phi_\lambda^*(i\downarrow)\phi_\mu^*(i\uparrow)][\phi_\nu(i\uparrow)\phi_\tau(i\downarrow) - \phi_\nu(i\downarrow)\phi_\tau(i\uparrow)] \\ & + \frac{1}{2}\sum_{\langle i\neq j\rangle,\sigma,\sigma'} U_{ij}[\phi_\lambda^*(i\sigma)\phi_\mu^*(j\sigma') - \phi_\lambda^*(j\sigma')\phi_\mu^*(i\sigma)][\phi_\nu(i\sigma)\phi_\tau(j\sigma') - \phi_\nu(j\sigma')\phi_\tau(i\sigma)] \ , \end{aligned} \tag{A12}$$

with the latter being symmetrized, $\langle\lambda\mu \mid V \mid \nu\tau\rangle = -\langle\mu\lambda \mid V \mid \nu\tau\rangle = -\langle\lambda\mu \mid V \mid \tau\nu\rangle = \langle\nu\tau \mid V \mid \lambda\mu\rangle^*$. The matrix elements of the electron-phonon term are given by

$$\bar{g}_{\lambda\mu}^k = \sum_{i,j,\sigma} \bar{g}_{ij}^k \phi_\lambda^*(i\sigma)\phi_\mu(j\sigma) \ , \tag{A13}$$

for which $\bar{g}_{\lambda\mu}^k = \bar{g}_{\mu\lambda}^{k*}$ holds.

The electronic part H_e is diagonalized as

$$H_e = \sum_\lambda \epsilon_\lambda N(c_\lambda^\dagger c_\lambda) \ , \tag{A14}$$

when the HF wave functions satisfy the HF equation

$$\begin{aligned} & \sum_{j(\neq i)} t_{ij}(\{\langle u_k\rangle\})\phi_\lambda(j\sigma) + e_i(\{\langle u_k\rangle\})\phi_\lambda(i\sigma) \\ & + \left(U_i\langle c_{i\bar{\sigma}}^\dagger c_{i\bar{\sigma}}\rangle + \sum_{j(\neq i),\sigma'} U_{ij}\langle c_{j\sigma'}^\dagger c_{j\sigma'}\rangle \right)\phi_\lambda(i\sigma) \\ & - U_i\langle c_{i\bar{\sigma}}^\dagger c_{i\sigma}\rangle\phi_\lambda(i\bar{\sigma}) - \sum_{j(\neq i),\sigma'} U_{ij}\langle c_{j\sigma'}^\dagger c_{i\sigma}\rangle\phi_\lambda(j\sigma') \\ & = \epsilon_\lambda\phi_\lambda(i\sigma) \ , \end{aligned} \tag{A15}$$

with self-consistently determined one-body densities,

$$\langle c_{i\sigma}^\dagger c_{j\sigma'}\rangle = \sum_{\lambda\in{\rm occ}} \phi_\lambda^*(i\sigma)\phi_\lambda(j\sigma') \ . \tag{A16}$$

The term linear in $\hat{u}_k$, H_z, is set to zero,

$$H_z = 0 \ , \tag{A17}$$

when the classical component of the lattice displacements, $\langle u_k \rangle$, satisfies the self-consistency conditions

$$\sum_{i,j,\sigma} \bar{g}^k_{ij} \langle c^\dagger_{i\sigma} c_{j\sigma} \rangle + \sum_l K_{kl} \langle u_l \rangle = 0 \ . \tag{A18}$$

With the above self-consistency conditions for the electronic and lattice parts, Eqs. (A15) and (A18), the constant term (HF total energy) H_c can be written in two equivalent ways,

$$\begin{aligned} H_c &= \sum_{i \neq j,\sigma} t_{ij}(\{\langle u_k \rangle\}) \langle c^\dagger_{i\sigma} c_{j\sigma} \rangle + \sum_{i,\sigma} e_i(\{\langle u_k \rangle\}) \langle c^\dagger_{i\sigma} c_{i\sigma} \rangle + \sum_i U_i (\langle c^\dagger_{i\uparrow} c_{i\uparrow} \rangle \langle c^\dagger_{i\downarrow} c_{i\downarrow} \rangle - \langle c^\dagger_{i\uparrow} c_{i\downarrow} \rangle \langle c^\dagger_{i\downarrow} c_{i\uparrow} \rangle) \\ &\quad + \sum_{\langle i \neq j \rangle,\sigma,\sigma'} U_{ij} (\langle c^\dagger_{i\sigma} c_{i\sigma} \rangle \langle c^\dagger_{j\sigma'} c_{j\sigma'} \rangle - \langle c^\dagger_{i\sigma} c_{j\sigma'} \rangle \langle c^\dagger_{j\sigma'} c_{i\sigma} \rangle) + \sum_{k,l} \frac{1}{2} K_{kl} \langle u_k \rangle \langle u_l \rangle \\ &= \sum_{\lambda \in \mathrm{occ}} \epsilon_\lambda - \sum_i U_i (\langle c^\dagger_{i\uparrow} c_{i\uparrow} \rangle \langle c^\dagger_{i\downarrow} c_{i\downarrow} \rangle - \langle c^\dagger_{i\uparrow} c_{i\downarrow} \rangle \langle c^\dagger_{i\downarrow} c_{i\uparrow} \rangle) - \sum_{\langle i \neq j \rangle,\sigma,\sigma'} U_{ij} (\langle c^\dagger_{i\sigma} c_{i\sigma} \rangle \langle c^\dagger_{j\sigma'} c_{j\sigma'} \rangle - \langle c^\dagger_{i\sigma} c_{j\sigma'} \rangle \langle c^\dagger_{j\sigma'} c_{i\sigma} \rangle) \\ &\quad + \sum_{k,l} \frac{1}{2} K_{kl} \langle u_k \rangle \langle u_l \rangle \ , \end{aligned} \tag{A19}$$

which can be used to check the self-consistency.

The phonon part H_p is diagonalized as

$$H_p = \sum_\nu \Omega_\nu (\zeta^\dagger_\nu \zeta_\nu + \tfrac{1}{2}) \ , \tag{A20}$$

with the transformation into the bare phonon operators

$$\hat{u_k} = \sum_\nu \frac{1}{\sqrt{2 M_k \Omega_\nu}} \Gamma_\nu(k) (\zeta_\nu + \zeta^\dagger_\nu) \ , \tag{A21}$$

$$p_k = \sum_\nu \sqrt{\frac{M_k \Omega_\nu}{2}} \Gamma_\nu(k) (-i\zeta_\nu + i\zeta^\dagger_\nu) \ , \tag{A22}$$

where the eigenfrequencies Ω_ν and their eigenfunctions $\Gamma_\nu(k)$ of the bare phonons are obtained by

$$\sum_l \frac{1}{\sqrt{M_k}} K_{kl} \frac{1}{\sqrt{M_l}} \Gamma_\nu(l) = \Omega^2_\nu \Gamma_\nu(k) \ . \tag{A23}$$

Finally, we rewrite the interaction part H_{int} into

$$\begin{aligned} H_{\mathrm{int}} &= \sum_{\lambda,\mu,\nu} g^\nu_{\lambda\mu} (\zeta_\nu + \zeta^\dagger_\nu) N(c^\dagger_\lambda c_\mu) \\ &\quad + \frac{1}{2} \sum_{\lambda\mu\nu\tau} \langle \lambda\mu \mid V \mid \nu\tau \rangle N(c^\dagger_\lambda c^\dagger_\mu c_\tau c_\nu) \ , \end{aligned} \tag{A24}$$

with

$$g^\nu_{\lambda\mu} = \sum_k \bar{g}^k_{\lambda\mu} \frac{1}{\sqrt{2 M_k \Omega_\nu}} \Gamma_\nu(k) \ , \tag{A25}$$

for which $g^\nu_{\lambda\mu} = g^{\nu *}_{\mu\lambda}$ holds.

APPENDIX B: RPA EQUATION FOR THE LINEAR FLUCTUATIONS AROUND THE MEAN-FIELD STATE

Here we call unoccupied and occupied HF eigenstates particle and hole *states*, respectively, and distinguish them:[35]

$$c_\lambda = p_\lambda \theta(\lambda - F) + h^\dagger_\lambda \theta(F - \lambda) \ , \tag{B1}$$

where $\theta(F-\lambda)$ takes unity if the orbital λ is occupied and zero otherwise. The word hole should not be confused with the previous "hole": Particle *states* here correspond to holes in the text and hole *states* to electrons as in "electron" doping. Creation and annihilation operators for a pair of particle and hole states,

$$\zeta^\dagger_{\lambda\mu} = p^\dagger_\lambda h^\dagger_\mu \ , \qquad \zeta_{\lambda\mu} = h_\mu p_\lambda \ , \tag{B2}$$

are regarded as boson operators, approximating their commutation relations by their expectation values in the HF states.

In terms of these operators and the bare phonon operators in Eq. (A20), the RPA consists in finding an operator

$$\begin{aligned} \xi^\dagger_n &= \sum_{\lambda > F > \mu} (\psi^{(n)*}_{\lambda\mu} \zeta^\dagger_{\lambda\mu} - \varphi^{(n)*}_{\lambda\mu} \zeta_{\lambda\mu}) \\ &\quad + \sum_\nu (\psi^{(n)*}_\nu \zeta^\dagger_\nu - \varphi^{(n)*}_\nu \zeta_\nu) \ , \end{aligned} \tag{B3}$$

such that its commutator with the Hamiltonian [Eq. (1)] approximately satisfies the relation

$$[H, \xi^\dagger_n] \simeq (E_n - E_0) \xi^\dagger_n \ . \tag{B4}$$

This is obtained by linearizing the equation of motion, e.g., with the use of

$$[N(c_\alpha^\dagger c_\beta^\dagger c_\delta c_\gamma), \zeta_{\lambda\mu}^\dagger] \simeq [(p_\alpha^\dagger h_\gamma^\dagger h_\beta p_\delta + p_\beta^\dagger h_\delta^\dagger h_\alpha p_\gamma - p_\alpha^\dagger h_\delta^\dagger h_\beta p_\gamma - p_\beta^\dagger h_\gamma^\dagger h_\alpha p_\delta + h_\alpha h_\beta p_\delta p_\gamma), p_\lambda^\dagger h_\mu^\dagger]$$
$$\simeq \delta_{\lambda\delta}\delta_{\mu\beta}(p_\alpha^\dagger h_\gamma^\dagger + h_\alpha p_\gamma) + \delta_{\lambda\gamma}\delta_{\mu\alpha}(p_\beta^\dagger h_\delta^\dagger + h_\beta p_\delta) - \delta_{\lambda\gamma}\delta_{\mu\beta}(p_\alpha^\dagger h_\delta^\dagger + h_\alpha p_\delta) - \delta_{\lambda\delta}\delta_{\mu\alpha}(p_\beta^\dagger h_\gamma^\dagger + h_\beta p_\gamma), \tag{B5}$$

where the indices α, β, γ, and δ denote HF eigenstates (not electron-lattice couplings). Straightforward algebra leads to the RPA equation

$$M \begin{pmatrix} \psi^{(n)*} \\ \varphi^{(n)*} \end{pmatrix} = (E_n - E_0) \begin{pmatrix} \psi^{(n)*} \\ -\varphi^{(n)*} \end{pmatrix} , \tag{B6}$$

where the vector denotes the coefficients in Eq. (B3),

$$\psi^{(n)*} = \begin{pmatrix} \psi_{\alpha\beta}^{(n)*} \\ \psi_\gamma^{(n)*} \end{pmatrix} , \quad \varphi^{(n)*} = \begin{pmatrix} \varphi_{\alpha\beta}^{(n)*} \\ \varphi_\gamma^{(n)*} \end{pmatrix} ,$$
$$(\alpha > F > \beta) . \tag{B7}$$

The matrix M is given by

$$M = \begin{pmatrix} \Omega + K_A & K_B \\ K_B^* & \Omega + K_A^* \end{pmatrix} , \tag{B8}$$

where the submatrices are given below. The matrix Ω is given by

$$\Omega = \begin{pmatrix} \Omega_{\lambda\mu;\alpha\beta} & \Omega_{\lambda\mu;\gamma} \\ \Omega_{\nu;\alpha\beta} & \Omega_{\nu;\gamma} \end{pmatrix} = \begin{pmatrix} \delta_{\lambda\alpha}\delta_{\mu\beta}(\epsilon_\lambda - \epsilon_\mu) & 0 \\ 0 & \delta_{\nu\gamma}\Omega_\nu \end{pmatrix} , \tag{B9}$$

where ϵ_λ denotes the HF energy level [Eq. (A15)] in Eq. (A14) and Ω_ν the bare phonon frequency [Eq. (A23)] in Eq. (A20). The matrices K_A and K_B are given by

$$K_A = \begin{pmatrix} K_{\lambda\mu;\alpha\beta}^A & K_{\lambda\mu;\gamma}^A \\ K_{\nu;\alpha\beta}^A & K_{\nu;\gamma}^A \end{pmatrix} = \begin{pmatrix} v_{\lambda\mu\alpha\beta}^* & g_{\lambda\mu}^\gamma \\ g_{\alpha\beta}^{\nu*} & 0 \end{pmatrix} , \tag{B10}$$

$$K_B = \begin{pmatrix} K_{\lambda\mu;\alpha\beta}^B & K_{\lambda\mu;\gamma}^B \\ K_{\nu;\alpha\beta}^B & K_{\nu;\gamma}^B \end{pmatrix} = \begin{pmatrix} u_{\lambda\mu\alpha\beta}^* & g_{\lambda\mu}^\gamma \\ g_{\alpha\beta}^\nu & 0 \end{pmatrix} , \tag{B11}$$

with

$$v_{\lambda\mu\alpha\beta}^* = 2\langle\lambda\beta \mid V \mid \mu\alpha\rangle , \quad u_{\lambda\mu\alpha\beta}^* = 2\langle\lambda\alpha \mid V \mid \mu\beta\rangle , \tag{B12}$$

where $\langle\lambda\mu \mid V \mid \nu\tau\rangle$ denotes the electron-electron interaction vertex [Eq. (A12)] and $g_{\lambda\mu}^\nu$ the electron-phonon interaction vertex [Eq. (A25)] in Eq. (A24).

An alternative diagrammatic derivation is presented in Appendix C. The HF excitation spectra and the bare phonon spectra are obtained by setting $K_A = K_B = 0$. With the relations $v_{\lambda\mu\alpha\beta}^* = v_{\alpha\beta\lambda\mu}$ and $u_{\lambda\mu\alpha\beta}^* = u_{\alpha\beta\lambda\mu}^*$, it is easily shown that the matrix K_A is Hermitian, K_B symmetric, and M Hermitian.[36] The approximate boson commutation relations follow from the normalization condition

$$\begin{pmatrix} \psi^{(n)*} \\ \varphi^{(n)*} \end{pmatrix}^\dagger \begin{pmatrix} \psi^{(m)*} \\ -\varphi^{(m)*} \end{pmatrix} = \delta_{nm}\mathrm{sgn}(E_n - E_0) . \tag{B13}$$

We can view the RPA equation, Eq. (B6), as the canonical transformation to diagonalize the effective boson Hamiltonian

$$H_{\mathrm{QB}} = H_c + \sum_\nu \frac{1}{2}\Omega_\nu + \sum_{l,a}[(\Omega + K_A)_{l;a}\zeta_l^\dagger\zeta_a + \tfrac{1}{2}(K_B)_{l;a}\zeta_l^\dagger\zeta_a^\dagger + \tfrac{1}{2}(K_B^*)_{l;a}\zeta_a\zeta_l]$$
$$(l = \lambda\mu, \nu;\ a = \alpha\beta, \gamma;\ \lambda > F > \mu;\ \alpha > F > \beta) . \tag{B14}$$

Here the first term is the total energy within the HF approximation for the electronic part and the classical approximation for the lattice part, as given in Eq. (A19). The second term represents the zero-point oscillation energy of the bare phonons. The diagonalization leads to

$$H_{\mathrm{QB}} = H_c + \sum_\nu \frac{1}{2}\Omega_\nu + E_{\mathrm{QB}} + \sum_{n;E_n>E_0}(E_n - E_0)\xi_n^\dagger\xi_n , \tag{B15}$$

where the correction to the HF total energy plus the bare phonon zero-point oscillation energy is given by

$$E_{\mathrm{QB}} = \frac{1}{2}\left[\sum_{n;E_n>E_0}(E_n - E_0) - \mathrm{tr}(\Omega + K_A)\right] . \tag{B16}$$

Note that this is the same with the diagrammatically derived RPA correction except the second-order term with respect to electron-electron interaction is counted twice in the above expression.[36]

The coefficients in Eq. (B3) denote matrix elements of the "bare" boson operators,

$$\psi_{\lambda\mu}^{(n)} = \langle n \mid \zeta_{\lambda\mu}^\dagger \mid 0\rangle , \quad \psi_\nu^{(n)} = \langle n \mid \zeta_\nu^\dagger \mid 0\rangle ,$$
$$\varphi_{\lambda\mu}^{(n)} = \langle n \mid \zeta_{\lambda\mu} \mid 0\rangle , \quad \varphi_\nu^{(n)} = \langle n \mid \zeta_\nu \mid 0\rangle , \tag{B17}$$

between the RPA ground and excited states,

$$\xi_n \mid 0\rangle = 0 , \quad \mid n\rangle = \xi_n^\dagger \mid 0\rangle . \tag{B18}$$

Any "two-body" Green's function is given, within the RPA, by substituting Eq. (B17) into its Lehmann representation. (Note that the Green's functions considered here are two body with respect to electron operators and one body with respect to phonon operators.) This allows the RPA Green's functions to satisfy energy-weighted sum rules[29] as long as the frequency integrations of the frequency-weighted Green's functions are evaluated in the RPA and the expectation values of the double commutator in the HF approximation.

APPENDIX C: DIAGRAMMATIC DERIVATION OF THE RPA EQUATION

Two-body Green's functions are defined by

$$\begin{aligned}\Pi(t)_{\lambda\mu;\alpha\beta} &= -i\langle 0 \mid T\zeta_{\lambda\mu}(t)\zeta^{\dagger}_{\alpha\beta} \mid 0\rangle \ , \\ \Pi(t)_{\lambda\mu;\gamma} &= -i\langle 0 \mid T\zeta_{\lambda\mu}(t)\zeta^{\dagger}_{\gamma} \mid 0\rangle \ , \\ \Pi(t)_{\lambda\mu;\overline{\alpha\beta}} &= -i\langle 0 \mid T\zeta_{\lambda\mu}(t)\zeta_{\alpha\beta} \mid 0\rangle \ , \\ \Pi(t)_{\lambda\mu;\overline{\gamma}} &= -i\langle 0 \mid T\zeta_{\lambda\mu}(t)\zeta_{\gamma} \mid 0\rangle \ , \ \text{etc.},\end{aligned} \tag{C1}$$

where the time-dependent operators are in the Heisenberg representation, and T denotes the time ordering. Their Fourier transforms are defined by

$$\Pi(\omega)_{\lambda\mu;\alpha\beta} = \int_{-\infty}^{\infty} dt\, e^{i\omega t}\Pi(t)_{\lambda\mu;\alpha\beta} \ , \ \text{etc.} \tag{C2}$$

Here the static part [the term proportional to $\delta(\omega)$] is not considered. The zeroth-order Green's functions are easily derived,

$$\begin{aligned}\Pi^0(\omega)_{\lambda\mu;\alpha\beta} &= \delta_{\lambda\alpha}\delta_{\mu\beta}\frac{1}{\omega-(\epsilon_\lambda-\epsilon_\mu)+i\eta} \ , \\ \Pi^0(\omega)_{\nu;\gamma} &= \delta_{\nu\gamma}\frac{1}{\omega-\Omega_\nu+i\eta} \ , \\ \Pi^0(\omega)_{\overline{\lambda\mu};\overline{\alpha\beta}} &= \delta_{\lambda\alpha}\delta_{\mu\beta}\frac{-1}{\omega+(\epsilon_\lambda-\epsilon_\mu)-i\eta} \ , \\ \Pi^0(\omega)_{\overline{\nu};\overline{\gamma}} &= \delta_{\nu\gamma}\frac{-1}{\omega+\Omega_\nu-i\eta} \ , \\ \Pi^0(\omega)_{\text{otherwise}} &= 0 \ ,\end{aligned} \tag{C3}$$

where η denotes an infinitesimal positive number. It will turn out immediately that the HF-orbital representation here is convenient since the inverse of $\Pi^0(\omega)$ is diagonal and linear in ω allowing numerically straightforward diagonalization to obtain all linear excitation modes.

We consider the Bethe-Salpeter equation for both particle-hole excitations and phonons with the interaction vertex whose order is lowest in H_{int}, as shown in Fig. 25. This can be written in a matrix form as

$$[\Pi(\omega)]^{-1} = [\Pi^0(\omega)]^{-1} - K \ , \tag{C4}$$

where the components of the matrix $\Pi(\omega)$,

$$\Pi(\omega) = \begin{pmatrix} \Pi(\omega)_{l;a} & \Pi(\omega)_{l;\overline{a}} \\ \Pi(\omega)_{\overline{l};a} & \Pi(\omega)_{\overline{l};\overline{a}} \end{pmatrix} \quad (l=\lambda\mu,\nu;\ a=\alpha\beta,\gamma) \ , \tag{C5}$$

are the Fourier transforms of Eq. (C1). From Eq. (C3), the inverse of $\Pi^0(\omega)$ takes the form

$$[\Pi^0(\omega)]^{-1} = \omega\begin{pmatrix} 1 & 0 \\ 0 & -1 \end{pmatrix} - \begin{pmatrix} \Omega & 0 \\ 0 & \Omega \end{pmatrix} \ , \tag{C6}$$

where the matrix Ω is given in Eq. (B9). It is straightforward to derive the kernel in the form

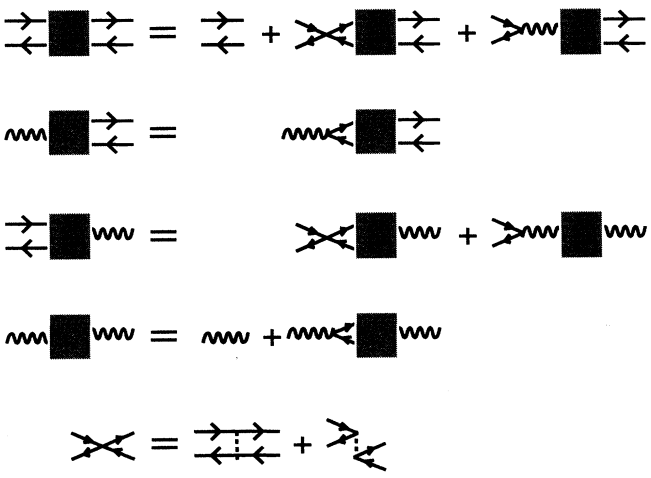

FIG. 25. Bethe-Salpeter equation for particle-hole excitations (a pair of solid lines) and phonons (wavy line). Electron-electron interaction vertex contains direct and exchange terms.

$$K = \begin{pmatrix} K_A & K_B \\ K_B^* & K_A^* \end{pmatrix} \ , \tag{C7}$$

whose matrix elements are given in Eqs. (B10) and (B11). Thus Eq. (B6) is rederived by setting

$$[\Pi(E_n - E_0)]^{-1}\begin{pmatrix} \psi^{(n)*} \\ \varphi^{(n)*} \end{pmatrix} = 0 \ . \tag{C8}$$

APPENDIX D: SOLUTION OF A GENERALIZED EIGENVALUE PROBLEM

In solving Eq. (B6) of the type

$$Mv_n = \omega_n\sigma_3 v_n \ , \tag{D1}$$

where σ_3 is one of the Pauli matrices, we first diagonalize the Hermitian matrix M to get

$$M = T\epsilon T^{\dagger} \ , \tag{D2}$$

where T is a unitary matrix and ϵ is a diagonal one. Then Eq. (D1) is reduced to another Hermitian problem,

$$(\epsilon^{-\frac{1}{2}}T^{\dagger}\sigma_3 T\epsilon^{-\frac{1}{2}})(\epsilon^{\frac{1}{2}}T^{\dagger}v_n) = \frac{1}{\omega_n}(\epsilon^{\frac{1}{2}}T^{\dagger}v_n) \ . \tag{D3}$$

When the HF state is stable, no element in ϵ is negative. For zero-frequency modes ($\omega_n = \epsilon_n = 0$), we added a very small positive number (10^{-10}) to ϵ_n in order to avoid numerical instability. Thus the zero-frequency modes have very small frequencies ($\omega_n \lesssim 10^{-5}$) and are treated in the same way as the other modes.

APPENDIX E: INTERACTION WITH RADIATION

Generally speaking, the model Hamiltonian [Eq. (1)] does not completely specify how the system interacts with photons [see (i) and (ii) below]. To see this, we first assume that the dipole moment is defined by

$$\mathbf{P}=\sum_i(\mathbf{r}_i+\mathbf{u}_i)\left(Z_i+\sum_\sigma c_{i\sigma}^\dagger c_{i\sigma}\right) \ , \tag{E1}$$

where $\mathbf{r}_i$ stands for the equilibrium positions of atoms, $\mathbf{u}_i$ for the lattice displacements, Z_i for the charge not explicitly included in the model, and $(Z_i+\sum_\sigma c_{i\sigma}^\dagger c_{i\sigma})$ for the ionic charge. We take $Z_i=+1$ for the Cu sites and $Z_i=-2$ for the O sites. Note that the vector notation $\mathbf{u}_i$ is used for the lattice displacements.

(i) Inclusion of $\mathbf{u}_i$ in $\mathbf{P}$ means that the ionic charge follows rigidly and instantaneously the motion of the corresponding atom. If the ionic charge is assumed *not* to follow the atomic motion, the dipole moment should be defined by $\mathbf{P}=\sum_i \mathbf{r}_i(Z_i+\sum_\sigma c_{i\sigma}^\dagger c_{i\sigma})$. In reality, the charge-density distribution around the atom would be distorted during the atomic motion and the center of the ionic charge would be different from the atomic position: The core charge would follow the atomic motion almost fully and with slight distortion, while the charge associated with the atomic orbital in the model would follow it partially and with large distortion.

(ii) Realistic values for Z_i would not be integers since the ionic charge is partially distributed into interstitial positions and other atomic positions.

Here we use Eq. (E1) for definition of the dipole moment. The paramagnetic current is derived through its time derivative

$$\mathbf{j}=i[H,\mathbf{P}]=i\sum_{i,j,\sigma}(\boldsymbol{\epsilon}_{ij}+\mathbf{u}_j-\mathbf{u}_i)t_{ij}(\{\mathbf{u}_k\})c_{i\sigma}^\dagger c_{j\sigma} +\sum_i\frac{\mathbf{p}_i}{M_i}\left(Z_i+\sum_\sigma c_{i\sigma}^\dagger c_{i\sigma}\right) \ , \tag{E2}$$

where $\boldsymbol{\epsilon}_{ij}=\mathbf{r}_j-\mathbf{r}_i$, and $\mathbf{p}_i$ denotes the conjugate momentum to $\mathbf{u}_i$.

The same paramagnetic current can be defined through a gauge transformation

$$c_{i\sigma}\rightarrow\exp\left(-i\frac{e}{c}\int^{\mathbf{r}_i+\mathbf{u}_i}\mathbf{A}\cdot d\boldsymbol{l}\right)c_{i\sigma} \ , \tag{E3}$$

$$\mathbf{p}_i\rightarrow\mathbf{p}_i-\frac{e}{c}\left(Z_i+\sum_\sigma c_{i\sigma}^\dagger c_{i\sigma}\right)\mathbf{A} \ ,$$

where e denotes charge of the carrier. The Hamiltonian is expanded as

$$H(\mathbf{A})-H(\mathbf{0})=-\frac{e}{c}\mathbf{j}\cdot\mathbf{A}+\frac{1}{2}\left(\frac{e}{c}\right)^2\mathbf{A}\cdot\overleftrightarrow{\boldsymbol{\tau}}\cdot\mathbf{A}+\cdots \ , \tag{E4}$$

and the first term gives the paramagnetic current. The stress tensor $\overleftrightarrow{\boldsymbol{\tau}}$ in the second term is given by

$$\overleftrightarrow{\boldsymbol{\tau}}=-\sum_{i,j,\sigma}(\boldsymbol{\epsilon}_{ij}+\mathbf{u}_j-\mathbf{u}_i)(\boldsymbol{\epsilon}_{ij}+\mathbf{u}_j-\mathbf{u}_i)t_{ij}(\{\mathbf{u}_k\})c_{i\sigma}^\dagger c_{j\sigma} +\sum_i\overleftrightarrow{\boldsymbol{I}}\frac{1}{M_i}\left(Z_i+\sum_\sigma c_{i\sigma}^\dagger c_{i\sigma}\right)^2 \ , \tag{E5}$$

where $\overleftrightarrow{\boldsymbol{I}}$ is a tensor such that $\mathbf{A}\cdot\overleftrightarrow{\boldsymbol{I}}\cdot\mathbf{A}=\mathbf{A}^2$. We add a comment concerning (i) after Eq. (E1).

(i') If the dipole moment is defined by $\mathbf{P}=\sum_i\mathbf{r}_i(Z_i+\sum_\sigma c_{i\sigma}^\dagger c_{i\sigma})$, then the paramagnetic current is $\mathbf{j}=i\sum_{i,j,\sigma}\boldsymbol{\epsilon}_{ij}t_{ij}(\{\mathbf{u}_k\})c_{i\sigma}^\dagger c_{j\sigma}$. This is equivalent to a gauge transformation $c_{i\sigma}\rightarrow\exp(-i\frac{e}{c}\int^{\mathbf{r}_i}\mathbf{A}\cdot d\boldsymbol{l})c_{i\sigma}$ (note the upper bound of the integration in the exponent) and $\mathbf{p}_i\rightarrow\mathbf{p}_i$, leading to the stress tensor $\overleftrightarrow{\boldsymbol{\tau}}=-\sum_{i,j,\sigma}\boldsymbol{\epsilon}_{ij}\boldsymbol{\epsilon}_{ij}t_{ij}(\{\mathbf{u}_k\})c_{i\sigma}^\dagger c_{j\sigma}$.

In view of the quasiboson picture of the RPA, the current operator, Eq. (E2), is linearized as

$$\mathbf{j}\simeq i\sum_{i,j,\sigma}(\boldsymbol{\epsilon}_{ij}+\langle\mathbf{u}_j\rangle-\langle\mathbf{u}_i\rangle)t_{ij}(\{\langle\mathbf{u}_k\rangle\})c_{i\sigma}^\dagger c_{j\sigma} +\sum_i\frac{\mathbf{p}_i}{M_i}\left(Z_i+\sum_\sigma\langle c_{i\sigma}^\dagger c_{i\sigma}\rangle\right) \ . \tag{E6}$$

In most cases, $\langle\mathbf{u}_j\rangle-\langle\mathbf{u}_i\rangle$ is much smaller than $\boldsymbol{\epsilon}_{ij}$. Then the current operator can be further approximated as

$$\mathbf{j}\simeq\mathbf{j}_{\rm el}+\mathbf{j}_{\rm ph} \ , \tag{E7}$$

where the electronic and phonon parts are given by

$$\mathbf{j}_{\rm el}=i\sum_{i,j,\sigma}\boldsymbol{\epsilon}_{ij}t_{ij}(\{\langle\mathbf{u}_k\rangle\})c_{i\sigma}^\dagger c_{j\sigma} \ , \tag{E8}$$

$$\mathbf{j}_{\rm ph}=\sum_i\frac{\mathbf{p}_i}{M_i}\left(Z_i+\sum_\sigma\langle c_{i\sigma}^\dagger c_{i\sigma}\rangle\right) \ . \tag{E9}$$

The above separation is convenient because the electronic and phonon parts scale differently [see Eq. (I20)]. For later convenience, we introduce

$$\mathbf{P}_{\rm ph}=\sum_i\hat{\mathbf{u}}_i\left(Z_i+\sum_\sigma\langle c_{i\sigma}^\dagger c_{i\sigma}\rangle\right) \ , \tag{E10}$$

which satisfies $\mathbf{j}_{\rm ph}=i[H,\mathbf{P}_{\rm ph}]$.

APPENDIX F: RPA EQUATION IN REAL SPACE

The real-space representation is sometimes more convenient since its basis is much smaller than the HF-orbital basis at the expense of more complicated frequency dependence. For later application to the IR absorption spectra, "two-body" Green's functions are given in a real-space representation:

$$\Pi(t)_{i\sigma i'\sigma';j\tau j'\tau'} = -i\langle 0 \mid Tc^{\dagger}_{i'\sigma'}(t)c_{i\sigma}(t)c^{\dagger}_{j\tau}c_{j'\tau'} \mid 0\rangle \ ,$$
$$\Pi(t)_{i\sigma i'\sigma';j} = -i\langle 0 \mid Tc^{\dagger}_{i'\sigma'}(t)c_{i\sigma}(t)\hat{u}_j \mid 0\rangle \ ,$$
$$\Pi(t)_{i;j\tau j'\tau'} = -i\langle 0 \mid T\hat{u}_i(t)c^{\dagger}_{j\tau}c_{j'\tau'} \mid 0\rangle \ ,$$
$$\Pi(t)_{i;j} = -i\langle 0 \mid T\hat{u}_i(t)\hat{u}_j \mid 0\rangle \ . \tag{F1}$$

The notation is similar to Eq. (C1). Their Fourier transforms are defined as in Eq. (C2). The zeroth-order Green's functions are obtained from Eq. (C3) through the transformations Eqs. (A2) and (A21). For example, the bare phonon part is given by

$$[\Pi^0(\omega)]^{-1}_{i;j} = \delta_{ij}M_i\omega^2 - K_{ij} \ , \tag{F2}$$

with the help of Eq. (A23). The interaction part $H_{\rm int}$ is written in the real-space representation as

$$H_{\rm int} = \sum_{i,j,k,\sigma} \bar{g}^k_{ij}\hat{u}_k N(c^{\dagger}_{i\sigma}c_{j\sigma}) + \sum_i U_i N(c^{\dagger}_{i\uparrow}c^{\dagger}_{i\downarrow}c_{i\downarrow}c_{i\uparrow}) + \sum_{\langle i\neq j\rangle,\sigma,\sigma'} U_{ij}N(c^{\dagger}_{i\sigma}c^{\dagger}_{j\sigma'}c_{j\sigma'}c_{i\sigma}) \ . \tag{F3}$$

Taking the same diagram (Fig. 25) with the same kernel (with the different representation) as in Appendix C, the Bethe-Salpeter equation is written as

$$[\Pi(\omega)]^{-1} = [\Pi^0(\omega)]^{-1} - K \ , \tag{F4}$$

where the components of the matrix $\Pi(\omega)$ are

$$\Pi(\omega) = \begin{pmatrix} \Pi_{EE}(\omega) & \Pi_{EP}(\omega) \\ \Pi_{PE}(\omega) & \Pi_{PP}(\omega) \end{pmatrix} = \begin{pmatrix} \Pi(\omega)_{i\sigma i'\sigma';j\tau j'\tau'} & \Pi(\omega)_{i\sigma i'\sigma';j} \\ \Pi(\omega)_{i;j\tau j'\tau'} & \Pi(\omega)_{i;j} \end{pmatrix} \ . \tag{F5}$$

The zeroth-order part is denoted for later use by

$$\Pi^0(\omega) = \begin{pmatrix} \Pi^0_{EE}(\omega) & 0 \\ 0 & \Pi^0_{PP}(\omega) \end{pmatrix} \ . \tag{F6}$$

Now the kernel takes the form

$$K = \begin{pmatrix} K_{EE} & K_{EP} \\ K_{PE} & 0 \end{pmatrix} \ , \tag{F7}$$

where

$$K_{EEi\sigma i'\sigma';j\tau j'\tau'} = \delta_{ii'jj'}(\delta_{\sigma\sigma'\bar{\tau}\bar{\tau}'} - \delta_{\sigma\bar{\sigma}'\tau\bar{\tau}'})U_i + (\delta_{ii'}\delta_{\sigma\sigma'}\delta_{jj'}\delta_{\tau\tau'} - \delta_{ij}\delta_{\sigma\tau}\delta_{i'j'}\delta_{\sigma'\tau'})U_{ij} \ ,$$
$$K_{EPi\sigma i'\sigma';j} = \delta_{\sigma\sigma'}\bar{g}^j_{ii'} \ ,$$
$$K_{PEi;j\tau j'\tau'} = \delta_{\tau\tau'}\bar{g}^{i*}_{jj'} \ , \tag{F8}$$

with $\delta_{ijkl} = 1$ if $i = j = k = l$ and $\delta_{ijkl} = 0$ otherwise.

It is straightforward to derive Eq. (F4) directly from Eq. (C4) also. Note that the basis for Eq. (C4) is larger than that for Eq. (F4). Equation (C4) is convenient since the inverse of $\Pi^0(\omega)$ in that representation is diagonal and linear in ω.

APPENDIX G: ELECTRON AND PHONON GREEN'S FUNCTIONS

For later convenience in the adiabatic approach, the electron-electron, the phonon-phonon, and the other components of the "two-body" Green's function are treated separately. Equation (F4) can be written as

$$[\Pi(\omega)]^{-1} = \begin{pmatrix} [\Pi_E(\omega)]^{-1} & 0 \\ 0 & [\Pi^0_{PP}(\omega)]^{-1} \end{pmatrix} - \begin{pmatrix} 0 & K_{EP} \\ K_{PE} & 0 \end{pmatrix} \ , \tag{G1}$$

where the electronically renormalized electron Green's function $\Pi_E(\omega)$ is given by

$$[\Pi_E(\omega)]^{-1} = [\Pi^0_{EE}(\omega)]^{-1} - K_{EE} \ , \tag{G2}$$

which is diagrammatically represented in Fig. 26. In the numerical computation, we used

$$\Pi_E(\omega) = \Pi^0_{EE}(\omega) + \Pi^0_{EE}(\omega)K_{EE}[1 - \Pi^0_{EE}(\omega)K_{EE}]^{-1}\Pi^0_{EE}(\omega) \ , \tag{G3}$$

to avoid the singularity of $[\Pi^0_{EE}(\omega)]^{-1}$ at $\omega = 0$.

With the use of $\Pi_E(\omega)$, the phonon-phonon component takes a simple form

$$[\Pi_{PP}(\omega)]^{-1} = [\Pi^0_{PP}(\omega)]^{-1} - K_{PE}\Pi_E(\omega)K_{EP} \ , \tag{G4}$$

which is diagrammatically represented in Fig. 27. The other components are also written, with the use of $\Pi_E(\omega)$ and $\Pi_{PP}(\omega)$, as

$$\Pi_{EE}(\omega) = \Pi_E(\omega) + \Pi_E(\omega)K_{EP}\Pi_{PP}(\omega)K_{PE}\Pi_E(\omega) \ , \tag{G5}$$

$$\Pi_{EP}(\omega) = \Pi_E(\omega)K_{EP}\Pi_{PP}(\omega) \ , \tag{G6}$$

$$\Pi_{PE}(\omega) = \Pi_{PP}(\omega)K_{PE}\Pi_E(\omega) \ , \tag{G7}$$

Equation (G5) is diagrammatically represented in Fig. 28.

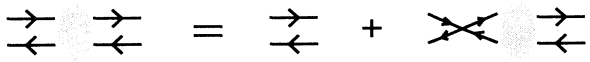

FIG. 26. Diagram for the electronically renormalized electron Green's function.

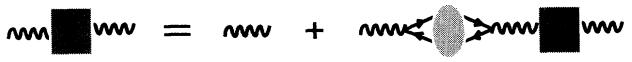

FIG. 27. Diagram for the (one-body) phonon Green's function.

APPENDIX H: ADIABATIC APPROXIMATION

When the adiabatic condition holds, the phonon-phonon component of the "two-body" Green's function (recall this is the one-body phonon Green's function) is well given by setting $\omega = 0$ in $\Pi_E(\omega)$ in Eq. (G4):

$$[\Pi_{PP}(\omega)]^{-1} \simeq [\Pi^A_{PP}(\omega)]^{-1} = [\Pi^0_{PP}(\omega)]^{-1} - K_{PE}\Pi_E(\omega=0)K_{EP} \ . \tag{H1}$$

With use of Eq. (F2) for $[\Pi^0_{PP}(\omega)]^{-1}$, this takes the form

$$[\Pi^A_{PP}(\omega)]^{-1}_{i;j} = \delta_{ij}M_i\omega^2 - K^{\rm ren}_{ij} \ , \tag{H2}$$

where the renormalized spring-constant matrix $K^{\rm ren}$ is defined by

$$K^{\rm ren} = K + K_{PE}\Pi_E(\omega=0)K_{EP} \ . \tag{H3}$$

Note that the matrix $K^{\rm ren}$ is real symmetric. Thus the adiabatic phonon Green's function is written as

$$[\Pi^A_{PP}(\omega)]_{i;j} = \frac{1}{\sqrt{M_i}}\sum_\nu \frac{\gamma_\nu(i)\gamma_\nu(j)}{\omega^2-\omega_\nu^2}\frac{1}{\sqrt{M_j}} \ , \tag{H4}$$

where the eigenfrequencies ω_ν and their eigenfunctions $\gamma_\nu(k)$ of the renormalized phonons are obtained by

$$\sum_l \frac{1}{\sqrt{M_k}}K^{\rm ren}_{kl}\frac{1}{\sqrt{M_l}}\gamma_\nu(l) = \omega_\nu^2\gamma_\nu(k) \ . \tag{H5}$$

APPENDIX I: CONDUCTIVITY

Conductivity is obtained from linear response theory by

$$\overleftrightarrow{\sigma}'(\omega>0) = -\frac{1}{\omega}\overleftrightarrow{R}''(\omega) \ , \tag{I1}$$

through the current-current correlation function

$$\overleftrightarrow{R}(\omega) = \langle\langle \mathbf{j};\mathbf{j}\rangle\rangle_\omega \ , \tag{I2}$$

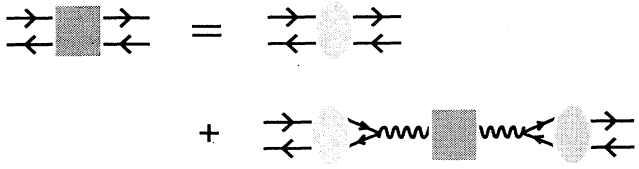

FIG. 28. Diagram for the two-body electron Green's function.

where $\langle\langle A;B\rangle\rangle_\omega$ denotes the Fourier transform of the Green's function, $-i\langle 0 \mid TA(t)B \mid 0\rangle/N_{\rm cell}$, with $N_{\rm cell}$ being the number of CuO_2 units and $A(t)$ in the Heisenberg representation. Single and double primes denote real and imaginary parts, respectively.

Conductivity can be derived also through the dipole-moment–dipole-moment correlation function

$$\overleftrightarrow{\sigma}'(\omega>0) = \omega\overleftrightarrow{\alpha}''(\omega) \ , \tag{I3}$$

with the polarizability

$$\overleftrightarrow{\alpha}(\omega) = -\langle\langle \mathbf{P};\mathbf{P}\rangle\rangle_\omega \ . \tag{I4}$$

Equations (I1) and (I3) are equivalent, as is easily shown with the use of $\mathbf{j} = \mathrm{i}[H,\mathbf{P}]$ and the Lehmann representation. Furthermore we can use

$$\overleftrightarrow{\sigma}'(\omega>0) = -\langle\langle \mathbf{j};\mathbf{P}\rangle\rangle'_\omega = \langle\langle \mathbf{P};\mathbf{j}\rangle\rangle'_\omega \ . \tag{I5}$$

The above relations also hold separately for the electronic and phonon parts of the current, so that we have

$$\begin{aligned}\overleftrightarrow{\sigma}'(\omega>0) &\simeq -\frac{1}{\omega}\langle\langle \mathbf{j}_{\rm el}+\mathbf{j}_{\rm ph};\mathbf{j}_{\rm el}+\mathbf{j}_{\rm ph}\rangle\rangle''_\omega \\ &= -\frac{1}{\omega}\langle\langle \mathbf{j}_{\rm el};\mathbf{j}_{\rm el}\rangle\rangle''_\omega - \langle\langle \mathbf{j}_{\rm el};\mathbf{P}_{\rm ph}\rangle\rangle'_\omega \\ &\quad +\langle\langle \mathbf{P}_{\rm ph};\mathbf{j}_{\rm el}\rangle\rangle'_\omega - \omega\langle\langle \mathbf{P}_{\rm ph};\mathbf{P}_{\rm ph}\rangle\rangle''_\omega \ ,\end{aligned} \tag{I6}$$

in which the last expression is convenient when the adiabatic approximation is used, and the middle one is useful otherwise.

Now we derive a formula for the conductivity in the phonon-frequency range within the adiabatic approximation, by treating terms in the last expression of Eq. (I6) separately. Using

$$\mathbf{j}_{\rm el} = \sum_{i,\sigma,j,\sigma'} \mathbf{J}_{i\sigma j\sigma'}c^\dagger_{i\sigma}c_{j\sigma'} \ , \tag{I7}$$

$$\mathbf{J}_{i\sigma j\sigma'} = i\delta_{\sigma\sigma'}\boldsymbol{\epsilon}_{ij}t_{ij}(\{\langle \mathbf{u}_k\rangle\}) \ , \tag{I8}$$

the electronic contribution is written as

$$\langle\langle \mathbf{j}_{\rm el};\mathbf{j}_{\rm el}\rangle\rangle_\omega = \frac{1}{N_{\rm cell}}\mathbf{J}^\dagger\Pi_{EE}(\omega)\mathbf{J} \ , \tag{I9}$$

where $\mathbf{J}^\dagger\Pi_{EE}(\omega)\mathbf{J}$ stands for

$$\sum_{i\sigma i'\sigma' j\tau j'\tau'} \mathbf{J}^*_{i\sigma i'\sigma'}\Pi_{EE}(\omega)_{i\sigma i'\sigma';j\tau j'\tau'}\mathbf{J}_{j\tau j'\tau'} \ .$$

This is divided into a purely electronic part $\langle\langle \mathbf{j}_{\rm el};\mathbf{j}_{\rm el}\rangle\rangle^H_\omega$ and a phonon-assisted part $\langle\langle \mathbf{j}_{\rm el};\mathbf{j}_{\rm el}\rangle\rangle^L_\omega$ where

$$\langle\langle \mathbf{j}_{\rm el};\mathbf{j}_{\rm el}\rangle\rangle^H_\omega = \frac{1}{N_{\rm cell}}\mathbf{J}^\dagger\Pi_E(\omega)\mathbf{J} \ , \tag{I10}$$

$$\langle\langle \mathbf{j}_{\rm el};\mathbf{j}_{\rm el}\rangle\rangle^L_\omega = \frac{1}{N_{\rm cell}}\mathbf{J}^\dagger\Pi_E(\omega)K_{EP}\Pi_{PP}(\omega)K_{PE}\Pi_E(\omega)\mathbf{J} \ , \tag{I11}$$

with the help of Eq. (G5).

In the insulating regime, where particle-hole pair excitation energy is much higher than phonon frequencies, the contribution from the purely electronic part is negligible in the phonon-frequency range. For the phonon-assisted part, we can use the adiabatic approximation $\Pi_{PP}(\omega) \rightarrow \Pi^A_{PP}(\omega)$. Because $K_{PE}\Pi_E(\omega=0)\mathbf{J}=0$, we need the first frequency derivative of $\Pi_E(\omega)$, $\partial_\omega \Pi_E(\omega=0)$, in Eq. (I11). Finally, the electronic contribution is given by

$$\langle\langle \mathbf{j}_{\rm el};\mathbf{j}_{\rm el}\rangle\rangle^L_\omega \simeq \frac{\omega^2}{N_{\rm cell}}\mathbf{J}^\dagger[\partial_\omega\Pi_E(\omega=0)]K_{EP} \times\Pi^A_{PP}(\omega)K_{PE}[\partial_\omega\Pi_E(\omega=0)]\mathbf{J} = \omega^2\sum_\nu \frac{\mathbf{F}^{\nu *}_{\rm el}\mathbf{F}^\nu_{\rm el}}{\omega^2-\omega^2_\nu} \ , \tag{I12}$$

where

$$\mathbf{F}^\nu_{\rm el} = \frac{1}{\sqrt{N_{\rm cell}}}\sum_{li\sigma i'\sigma' j\tau j'\tau'} \gamma_\nu(l)\frac{1}{\sqrt{M_l}}K_{PEl;i\sigma i'\sigma'}[\partial_\omega\Pi_E(\omega=0)]_{i\sigma i'\sigma';j\tau j'\tau'}\mathbf{J}_{j\tau j'\tau'} \ . \tag{I13}$$

The quantity $\mathbf{F}^\nu_{\rm el}$ is pure imaginary. It is straightforward to show that $\partial_\omega\Pi_{\rm E}(\omega)$ is given by

$$\partial_\omega\Pi_E(\omega) = [1+\Pi_E(\omega)K_{EE}]\partial_\omega\Pi^0_{EE}(\omega)[1+K_{EE}\Pi_E(\omega)] \ . \tag{I14}$$

The phonon contribution is written as

$$\langle\langle \mathbf{P}_{\rm ph};\mathbf{P}_{\rm ph}\rangle\rangle_\omega \simeq \frac{1}{N_{\rm cell}}\sum_{ij}\epsilon_i\left(Z_i+\sum_\sigma\langle c^\dagger_{i\sigma}c_{i\sigma}\rangle\right) \times\Pi^A_{PP}(\omega)_{i;j}\left(Z_j+\sum_\tau\langle c^\dagger_{j\tau}c_{j\tau}\rangle\right)\epsilon_j = \sum_\nu\frac{\mathbf{F}^{\nu *}_{\rm ph}\mathbf{F}^\nu_{\rm ph}}{\omega^2-\omega^2_\nu} \ , \tag{I15}$$

where a polarization vector $\boldsymbol{\epsilon}_i$ is defined by $\hat{\mathbf{u}}_i = \hat{u}_i\boldsymbol{\epsilon}_i$, and

$$\mathbf{F}^\nu_{\rm ph} = \frac{1}{\sqrt{N_{\rm cell}}}\sum_j\gamma_\nu(j)\frac{1}{\sqrt{M_j}}\left(Z_j+\sum_\tau\langle c^\dagger_{j\tau}c_{j\tau}\rangle\right)\epsilon_j \ . \tag{I16}$$

The quantity $\mathbf{F}^\nu_{\rm ph}$ is real.

Similarly, we obtain the electron-phonon cross-term contributions,

$$\langle\langle \mathbf{j}_{\rm el};\mathbf{P}_{\rm ph}\rangle\rangle_\omega \simeq \frac{1}{N_{\rm cell}}\sum_{i\sigma i'\sigma' j}\mathbf{J}^*_{i\sigma i'\sigma'}\Pi_{EP}(\omega)_{i\sigma i'\sigma';j} \times\left(Z_j+\sum_\tau\langle c^\dagger_{j\tau}c_{j\tau}\rangle\right)\epsilon_j \simeq \omega\sum_\nu\frac{\mathbf{F}^{\nu *}_{\rm el}\mathbf{F}^\nu_{\rm ph}}{\omega^2-\omega^2_\nu} \ , \tag{I17}$$

$$\langle\langle \mathbf{P}_{\rm ph};\mathbf{j}_{\rm el}\rangle\rangle_\omega \simeq \frac{1}{N_{\rm cell}}\sum_{ij\tau j'\tau'}\epsilon_i\left(Z_i+\sum_\sigma\langle c^\dagger_{i\sigma}c_{i\sigma}\rangle\right) \times\Pi_{PE}(\omega)_{i;j\tau j'\tau'}\mathbf{J}_{j\tau j'\tau'} \simeq \omega\sum_\nu\frac{\mathbf{F}^{\nu *}_{\rm ph}\mathbf{F}^\nu_{\rm el}}{\omega^2-\omega^2_\nu} \ , \tag{I18}$$

with the help of Eqs. (G6) and (G7).

Finally, using Eq. (I6), we obtain the formula

$$\overleftrightarrow{\sigma}'(\omega>0) \simeq \frac{\pi}{2}\sum_\nu\delta(\omega-\omega_\nu)(\mathbf{F}^\nu_{\rm ph}-i\mathbf{F}^\nu_{\rm el})^*(\mathbf{F}^\nu_{\rm ph}-i\mathbf{F}^\nu_{\rm el}) \ . \tag{I19}$$

It is easily shown that a simple scaling law holds for the conductivity, within the adiabatic approximation used here. Two sets of parameters, only differing by $\bar{g}^k_{ij} = s\bar{g'}^k_{ij}$ and $K_{kl} = s^2K'_{kl}$ (s a real number), give the same HF configuration for charge and spin densities. The lattice displacements are related by $\langle u_k\rangle = s^{-1}\langle u'_k\rangle$ and the renormalized phonon frequencies by $\omega_\nu = \mid s \mid \omega'_\nu$. When Eq. (E7) is used for the current operator, the conductivities are related by

$$\overleftrightarrow{\sigma}'(\omega>0) \simeq \frac{\pi}{2}\sum_\nu\delta(\omega-\mid s\mid\omega'_\nu)(\mathbf{F}'^\nu_{\rm ph}-is\mathbf{F}'^\nu_{\rm el})^*(\mathbf{F}'^\nu_{\rm ph}-is\mathbf{F}'^\nu_{\rm el}) \ . \tag{I20}$$

*Present address: International Center for Theoretical Physics, Strada Costiera 11, 34014 Trieste, Italy.
†Present address: Laboratory of Applied and Solid State Physics, University of Groningen Nijenborgh 4, 9747 AG Groningen, The Netherlands.

[1]D. Vaknin, S. K. Sinha, D. E. Moncton, D. C. Johnston, J. M. Newsam, C. R. Safinya, and H. E. King, Jr., Phys. Rev. Lett. **58**, 2802 (1987); Y. J. Uemura, W. J. Kossler, X. H. Yu, J. R. Kempton, H. E. Schone, D. Opie, C. E. Stronach, D. C. Johnston, M. S. Alvarez, and D. P. Goshorn, *ibid.* **59**, 1045 (1987); G. Shirane, Y. Endoh, R. J. Birgeneau, M. A. Kastner, Y. Hidaka, M. Oda, M. Suzuki, and T. Murakami, *ibid.* **59**, 1613 (1987).
[2]P. W. Anderson, Science **235**, 1196 (1987).
[3]V. J. Emery, Phys. Rev. Lett. **58**, 2794 (1987); J. E. Hirsch, *ibid.* **59**, 228 (1987); C. M. Varma, S. Schmitt-Rink, and E. Abrahams, Solid State Commun. **62**, 681 (1987).
[4]J. Wagner, W. Hanke, and D. J. Scalapino, Phys. Rev. B **43**, 10517 (1991).
[5]For recent numerical works, see G. Dopf, A. Muramatsu, and W. Hanke, Phys. Rev. Lett. **68**, 353 (1992); G. Dopf, J. Wagner, P. Dieterich, A. Muramatsu, and W. Hanke, *ibid.* **68**, 2082 (1992), and references therein.
[6]M. D. Nuñez Regueiro and A. A. Aligia, Phys. Rev. Lett. **61**, 1889 (1988).
[7]J. Zhong and H. B. Schüttler, Phys. Rev. Lett. **69**, 1600 (1992).
[8]For recent works, see C. Di Castro, L. F. Feiner, and M. Grilli, Phys. Rev. Lett. **66**, 3209 (1991); L. F. Feiner, M. Grilli, and C. Di Castro, Phys. Rev. B **45**, 10647 (1992), and references therein.
[9]K. Yonemitsu, A. R. Bishop, and J. Lorenzana, Phys. Rev. Lett. **69**, 965 (1992).
[10]J. E. Hirsch, E. Loh, Jr., D. J. Scalapino, and S. Tang, Phys. Rev. B **39**, 243 (1989); S. A. Trugman, Phys. Scr. T **27**, 113 (1989).
[11]Z. Tešanović, A. R. Bishop, and R. L. Martin, Solid State Commun. **68**, 337 (1988); P. B. Littlewood, C. M. Varma, S. Schmitt-Rink, and E. Abrahams, Phys. Rev. B **39**, 12371 (1989).
[12]J. Lorenzana and L. Yu, Phys. Rev. B **43**, 11474 (1991); Mod. Phys. Lett. B **5**, 1515 (1991).
[13]V. I. Anisimov, M. A. Korotin, J. Zaanen, and O. K. Andersen, Phys. Rev. Lett. **68**, 345 (1992).
[14]J. B. Grant and A. K. McMahan, Phys. Rev. B **46**, 8440 (1992).
[15]G. A. Thomas, D. H. Rapkine, S. L. Cooper, S-W. Cheong, and A. S. Cooper, Phys. Rev. Lett. **67**, 2906 (1991).
[16]Y. H. Kim, S-W. Cheong, and Z. Fisk, Phys. Rev. Lett. **67**, 2227 (1991); G. Yu, C. H. Lee, A. J. Heeger, N. Herron, and E. M. McCarron, *ibid.* **67**, 2581 (1991) ; C. Taliani, A. J. Pal, G. Ruani, R. Zamboni, X. Wei, and Z. V. Vardeny, in *Electronic Properties of High-T_c Superconductors and Related Compounds*, edited by H. Kuzmany, M. Mehring, and J. Fink (Springer-Verlag, Berlin, 1990), and references therein.
[17]J. E. Hirsch, Phys. Rev. B **35**, 8726 (1987); F. C. Zhang and P. Prelovsek, *ibid.* **37**, 1569 (1988); S. Tang and J. E. Hirsch, *ibid.* **37**, 9546 (1988).
[18]K. Yonemitsu, A. R. Bishop, and J. Lorenzana, Phys. Rev. B **47**, 8065 (1993).
[19]For recent studies, see, for example, A. Singh and Z. Tešanović, Phys. Rev. B **41**, 614 (1990); J. A. Vergés, E. Louis, P. S. Lomdahl, F. Guinea, and A. R. Bishop, *ibid.* **43**, 6099 (1991); M. Inui and P. B. Littlewood, *ibid.* **44**, 4415 (1991).
[20]J. Zaanen and O. Gunnarsson, Phys. Rev. B **40**, 7391 (1989).
[21]K. Yonemitsu, I. Batistić, and A. R. Bishop, Phys. Rev. B **44**, 2652 (1991).
[22]K. Yonemitsu and A. R. Bishop, Phys. Rev. B **45**, 5530 (1992).
[23]C. A. Balseiro, A. G. Rojo, E. R. Gagliano, and B. Alascio, Phys. Rev. B **38**, 9315 (1988); E. R. Gagliano and C. A. Balseiro, *ibid.* **38**, 11766 (1988).
[24]J. Lorenzana, M. D. Grynberg, L. Yu, K. Yonemitsu, and A. R. Bishop, Phys. Rev. B (to be published).
[25]M. S. Hybertsen, M. Schlüter, and N. E. Christensen, Phys. Rev. B **39**, 9028 (1989); A. K. McMahan, J. F. Annett, and R. M. Martin, *ibid.* **42**, 6268 (1990).
[26]F. C. Zhang and T. M. Rice, Phys. Rev. B **37**, 3759 (1988).
[27]H. Matsukawa and H. Fukuyama, J. Phys. Soc. Jpn. **58**, 3687 (1989).
[28]J. R. Schrieffer, X.-G. Wen, and S.-C. Zhang, Phys. Rev. Lett. **60**, 944 (1988); Phys. Rev. B **39**, 11663 (1989).
[29]D. J. Thouless, Nucl. Phys. **22**, 78 (1961).
[30]M. J. Rice and Y. R. Wang, Phys. Rev. B **36**, 8794 (1987).
[31]I. Batistić and A. R. Bishop, Phys. Rev. B **45**, 5282 (1992).
[32]H. Ito and Y. Ono, J. Phys. Soc. Jpn. **54**, 1194 (1985); A. Terai, Y. Ono, and Y. Wada, *ibid.* **55**, 2889 (1986); K. Yonemitsu, Y. Ono, and Y. Wada, *ibid.* **56**, 4400 (1987).
[33]P. Y. Le Daeron and S. Aubry, J. Phys. C **16**, 4827 (1983); J. Phys. (Paris) Colloq. **44**, C3-1573 (1983).
[34]I. Batistić, A. R. Bishop, R. L. Martin, and Z. Tešanović, Phys. Rev. B **40**, 6896 (1989); J. Mustre de Leon, I. Batistić, A. R. Bishop, S. D. Conradson, and S. A. Trugman, Phys. Rev. Lett. **68**, 3236 (1992).
[35]A. L. Fetter and J. D. Walecka, *Quantum Theory of Many-Particle Systems* (McGraw-Hill, New York, 1971), Chap. 15.
[36]J.-P. Blaizot and G. Ripka, *Quantum Theory of Finite Systems* (MIT Press, Cambridge, MA, 1986); for the mathematical properties of Eq. (B6), see Sec. 3.2; for the relation with the diagrammatic method, see also Sec. 15.9.